Supplementary Information (SI) for Energy & Environmental Science.
This journal is © The Royal Society of Chemistry 2024

Electronic Supplementary Information

High-entropy perovskite fluoride ultrasmall nanoparticles embedded in carbon nanofibers enable accelerated redox kinetic for K storage

Jiaying Liao,[a] Caoyang Shao,[b] Jingchen Han,[a] Zeyu Yuan,[a] Qiao Hu,[c] Yichen Du,[a] Shaohua Guo,[b] Xiaosi Zhou*[a] and Haoshen Zhou*[b]

[a] School of Chemistry and Materials Science, Nanjing Normal University, Nanjing 210023, China

[b] College of Engineering and Applied Sciences, National Laboratory of Solid State Microstructures, Nanjing University, Nanjing 210093, China

[c] College of Chemical Engineering, Nanjing Forestry University, Nanjing 210037, China

*Corresponding authors: zhouxiaosi@njnu.edu.cn; hszhou@nju.edu.cn.

Experimental section

Materials. Magnesium acetate tetrahydrate ($Mg(Ac)_2·4H_2O$), aluminum acetylacetonate ($Al(acac)_3$), potassium fluoride (KF), potassium acetate (KAc), calcium acetate monohydrate ($Ca(Ac)_2·H_2O$), scandium acetylacetonate ($Sc(acac)_3$), titanium oxide acetylacetonate ($TiO(acac)_2$), vanadium acetylacetonate ($V(acac)_3$), chromium acetate ($Cr(Ac)_3$), manganese acetate tetrahydrate ($Mn(Ac)_2·4H_2O$), iron acetate ($Fe(Ac)_2$), iron acetylacetonate ($Fe(acac)_3$), iron chloride tetrahydrate ($FeCl_2·4H_2O$), cobalt acetate tetrahydrate ($Co(Ac)_2·4H_2O$), nickel acetate tetrahydrate ($Ni(Ac)_2·4H_2O$), copper acetate monohydrate ($Cu(Ac)_2·H_2O$), zinc acetate dihydrate ($Zn(Ac)_2·2H_2O$), gallium acetylacetonate ($Ga(acac)_3$), *N*,*N*-dimethylformamide (DMF), glucose, and polyvinylidene fluoride (PVDF, M_w ~ 534,000) were purchased from Aladdin. All the chemicals were used without further purification.

Preparation of HE-KMF_3@CNFs. First, 2 mmol KAc, 2 mmol equimolar transition metal salts (0.4 mmol $Mg(Ac)_2·4H_2O$, 0.4 mmol $Mn(Ac)_2·4H_2O$, 0.4 mmol $Fe(Ac)_2$, 0.4 mol $Co(Ac)_2·4H_2O$, 0.4 mol $Ni(Ac)_2·4H_2O$), and 1 g PVDF were dissolved in 10 mL DMF, under vigorous stirring, at 50 ℃ for 6 h. The resultant homogeneous solution was drawn into a 10 mL syringe equipped with a 20-gauge blunt-tip needle and used as the precursor fluid for electrospinning. Al foil was used as the current collector, and the distance between the needle tip and Al foil was adjusted to 17 cm. Subsequently, a direct-current power supply was employed to provide a voltage of 20 kV between the Al foil and needle tip. The flow velocity was controlled at 0.5 mL h^{-1} by a syringe pump. Finally, the as-spun membranes were heated in an electric oven at 150 ℃ for 1 h and sintered in a tube furnace at 500 ℃ for 3 h under flowing argon to obtain HE-KMF_3@CNFs.

Preparation of KMF_3@CNFs (M = Mg, Ca, Mn, Fe, Co, Ni, Cu, Zn). 2 mmol KAc, 2 mmol transition metal acetate salt $M(Ac)_2·xH_2O$, and 1 g PVDF were dissolved in 10 mL DMF at 50 ℃ by vigorous stirring for 6 h. The resulting homogeneous solution was used as the precursor fluid for electrospinning by loading it into a 10 mL syringe equipped with a 20-gauge blunt tip needle. Al foil was used as a current collector, and the distance between the needle tip and the Al foil was tuned to 17 cm. After that, a direct-current power supply was used to provide a voltage of 20 kV between the

Al foil and the needle tip. The flow rate was controlled at 0.5 mL h^{-1} by a syringe pump. Finally, the as-spun membrane was heated in an electric oven at 150 ℃ for 1 h and pyrolyzed in a tube furnace at 500 ℃ for 3 h under an Ar environment to obtain KMF_3@CNFs.

Preparation of K_3MF_6@CNFs (M = Al, Sc, Ti, V, Cr, Ga). 3 mmol KAc, 1 mmol transition metal acetylacetonate (or acetate) salt, and 1 g PVDF were dissolved in 10 mL DMF at 50 ℃ by continuous stirring for 6 h. The electrospinning and pyrolysis processes are the same as those of KMF_3@CNFs.

Preparation of high-entropy-KMF_3 via coprecipitation (HE-KMF_3-CP). HE-KMF_3-CP was synthesized based on a previously reported method.[1] 20 mmol equimolar transition metal salts (4 mmol $Mg(Ac)_2{\cdot}4H_2O$, 4 mmol $Mn(Ac)_2{\cdot}4H_2O$, 4 mmol $Fe(Ac)_2$, 4 mol $Co(Ac)_2{\cdot}4H_2O$, and 4 mol $Ni(Ac)_2{\cdot}4H_2O$) were ground by a planetary ball for 10 min. Then, 60 mmol KF was dissolved in 10 mL deionized water at 100 ℃. The ball-milled transition metal salts were poured into the KF solution and heated continuously for 10 min. The precipitate was isolated by a vacuum filtration process, washed by deionized water, and dried under vacuum at 80 ℃.

Preparation of HE-KMF_3 via electrospinning (HE-KMF_3-ES). The HE-KMF_3@CNFs obtained by electrospinning were annealed in a muffle furnace at 500 ℃ for 1 h under an air environment to remove carbon and obtain HE-KMF_3-ES nanoparticles.

Preparation of HE-KMF_3@C. 2 mmol KAc, 2 mmol equimolar transition metal salts (0.4 mmol $Mg(Ac)_2{\cdot}4H_2O$, 0.4 mmol $Mn(Ac)_2{\cdot}4H_2O$, 0.4 mmol $Fe(acac)_3$, 0.4 mol $Co(Ac)_2{\cdot}4H_2O$, and 0.4 mol $Ni(Ac)_2{\cdot}4H_2O$), and 1 g PVDF were dissolved in 10 mL DMF at 50 ℃ with vigorous stirring for 6 h. The resultant homogeneous solution was heated in an oil bath at 150 ℃ for 2 h under stirring to evaporate DMF. The as-obtained powder was sintered in a tube furnace at 500 ℃ for 3 h under flowing argon to obtain HE-KMF_3@C.

Preparation of $KFeF_3$ nanoparticles. 2 mmol $FeCl_2{\cdot}4H_2O$ and 6 mmol KF were dissolved in 50 mL ethylene glycol. The resulting clear solution was poured into a 100 mL Teflon-lined stainless-steel autoclave and sealed. Subsequently, the autoclave was kept in an electric oven at 160 ℃ for 6 h. After cooling, the precipitate was harvested by centrifugation, washed three times with ethanol, and dried in a vacuum oven at 80 ℃ overnight to obtain $KFeF_3$ nanoparticles.

Preparation of hard carbon spheres (HCS). HCS was fabricated according to a previously reported approach.[2] In a typical synthesis, 4.8 g glucose was dissolved in 30 mL deionized water, and the resulting clear solution was poured into a 40 mL Teflon-lined stainless-steel autoclave and sealed. Then, the autoclave was kept in an electric oven at 195 ℃ for 6 h. After cooling, the precipitate was collected by centrifugation and washed three times with deionized water. The obtained precipitate was then dried in a vacuum oven at 80 ℃ overnight and annealed in a tube furnace at 900 ℃ for 6 h in an Ar atmosphere to obtain HCS.

Characterization. The morphology and microstructure were investigated by field-emission scanning electron microscope (FESEM; JSM-7600F) and transmission electron microscope (TEM; FEI Talos F200X). Elemental distribution and energy-dispersive X-ray spectroscopy (EDX) spectra were acquired on the FEI Talos F200X TEM equipped with a high-brightness field emission gun (X-FEG) and a Super-X G2 EDX detector. High-angle annular dark-field (HAADF) imaging was performed on a Titan G2 60-300 Cubed scanning transmission electron microscope (STEM) fitted with dual aberration correctors for probe formation and imaging lenses. The elemental ratios of the synthesized materials were evaluated by inductively coupled plasma (ICP; Shimadzu, ICPS-8100). The crystal structure was studied by X-ray diffraction (XRD; Rigaku, SmartLab). Thermogravimetric analysis (TGA) was conducted on a NETZSCH STA 449 F3 thermogravimetric analyzer in air at a heating rate of 10 ℃ min^{-1}. Raman spectra were recorded on a HORIBA LabRAM HR Evolution using a 532 nm laser as the excitation source. X-ray photoelectron spectroscopy (XPS) spectra were measured on an ESCALAB Xi+ electron spectrometer to determine element information and valence. *In situ* XRD patterns were obtained using an X'Pert Pro MPD X-ray diffractometer (D8 Bruker Advance, Germany) equipped with Cu-Kα radiation (λ = 1.5406 Å) at 40 kV and 40 mA.

Electrochemical measurements. Electrochemical characterization was performed using CR2032 coin cells. The HE-KMF_3@CNFs, KMF_3@CNFs, HE-KMF_3-CP, or HE-KMF_3-ES electrode was prepared by mixing the active materials (80 wt%), super-P carbon black (10 wt%), and PVDF binder (10 wt%) in N-methyl-2-pyrrolidinone to form a uniform slurry, which was pasted on Al foil and then dried in a vacuum oven at 80 ℃ for 12 h. The typical loading mass of active material is approximately 1.5 mg cm^{-2}. HE-KMF_3@CNFs film can also be directly cut into slices as free-standing electrodes,

with different mass loading of approximately 5.0, 7.7, and 10.8 mg cm^{-2}. Potassium foil and glass fiber (Whatman) were used as counter/reference electrode and separator, respectively. The electrolyte was 3 M potassium bis(fluorosulfonyl) imide (KFSI) in triethyl phosphate (TEP). All batteries were assembled in an argon-filled glovebox (MBRAUN) with H_2O and O_2 levels below 0.1 ppm. Galvanostatic charge/discharge tests were conducted on a Land CT2001A battery test system with a voltage range of 1.5–4.5 V. Note that for the calculation of specific capacity, the mass of CNFs was not excluded. Cyclic voltammetry (CV) and galvanostatic intermittent titration technique (GITT) characterizations were carried out on a PARSTAT 4000 electrochemical workstation. For the GITT investigation, the batteries were charged/discharged with a pulsed current of 20 mA g^{-1} for 10 min, followed by a 4 h relaxation to reach the potassium equilibrium potential.

To construct a potassium-ion full battery, HCS was chosen as the anode material. The anode was prepared by mixing HCS, super-P carbon black, and carboxymethyl cellulose (CMC) binder in a weight ratio of 80:10:10. The resulting slurry was coated on Al foil and dried in a vacuum oven at 80 ℃ for 12 h. The representative loading mass of active material is around 1.0 mg cm^{-2}. The electrolyte was 3 M KFSI in TEP. Before full-cell assembly, the HCS electrodes were pre-cycled between 0.01 and 1.5 V in half-cells to remove the irreversible capacities in the first few cycles. In order to achieve the best energy and power density of the full battery, the capacity ratio of the cathode to the anode is approximately 0.9.

Conductivity tests. For the investigation of electronic conductivity, the as-synthesized powder samples were pelletized at a pressure of 20 MPa. A typical pellet had a diameter of 14 mm and a thickness of about 1.0 mm. Silver conductive paste was then pasted on both sides of the bare $KFeF_3$ and HE-KMF_3-ES pellets as electronic electrodes. Electronic conductivity measurements of $KFeF_3$ and HE-KMF_3-ES pellets were performed at different voltages from 1.0 to 5.0 V under potentiostatic conditions. Electronic conductivity measurements of $KFeF_3$@CNFs and HE-KMF_3@CNFs pellets were performed by an M-3 Mini type four-probe tester.

Theoretical calculations. The simulation calculations for HE-KMF_3 and $KFeF_3$ were performed with density function theory by the Vienna ab initio simulation package and the projector-augmented wave method. Electron exchange-correlation interaction effects were generalized by gradient

approximation with Perdew-Burke-Ernzerhof exchange-correlation function. In order to optimize the model structure, the plane wave basis set was set to a kinetic energy cutoff of 500 eV. The electron energy convergence condition was set to less than 10^{-6} eV and a force relaxation of 0.02 eV $Å^{-1}$ was adopted. During geometry optimization, all atomic positions were allowed to relax. The *k*-points for HE-KMF_3 and $KFeF_3$ bulk were set to 3*3*3. The transition state search used the climbing-image nudged elastic band (CI-NEB) method of the variational transition-state theory tool. The CI-NEB calculation converged when the force in each image was below 0.05 eV $Å^{-1}$.

The (100), (110), (111), and (211) surface energies with different element exposures were calculated according to the following equation:[3]

$$E_{surf} = \frac{E_{slab} - N * E_{bulk}}{2A} \quad (1)$$

where E_{surf} is the surface energy, E_{slab} is the energy after bulk cleaving, N is the number of bulk structures in the unit slab structure, E_{bulk} is the bulk energy of HE-KMF_3 or $KFeF_3$, and A is the surface area of (100), (110), (111), or (211).

$E_{adsorption}$ was calculated as $E_{adsorption} = E_{total} - E_{ads} - E_{sub}$, where E_{total} and E_{sub} are the energies with and without adsorbate, and E_{ads} is the energy of adsorbate in the empty box. The differential charge density was calculated by the following equation:[4]

$$\Delta\rho = \rho_{tot} - \rho_{sub} - \rho_{ad} \quad (2)$$

where ρ_{tot}, ρ_{sub}, and ρ_{ad} denote the total charge density, substrate charge density, and charge density of the absorbed graphite layer, respectively. Blue areas indicate charge depletion and the yellow areas indicate charge accumulation.

The Gibbs reaction free energy of the conversion reaction can be expressed as the following equation:[5]

$$\Delta G_{reaction} = G_{product} - G_{reactant} \quad (3)$$

where $\Delta G_{reaction}$ is the Gibbs reaction free energy change of the conversion reaction. $G_{product}$ is the Gibbs free energy at 298 K for bulk Fe, Mn, Co, Mg, Ni, and KF, and $G_{reactant}$ is the Gibbs free energy at 298 K for $KFeF_3$, HE-KMF_3, and K^+.

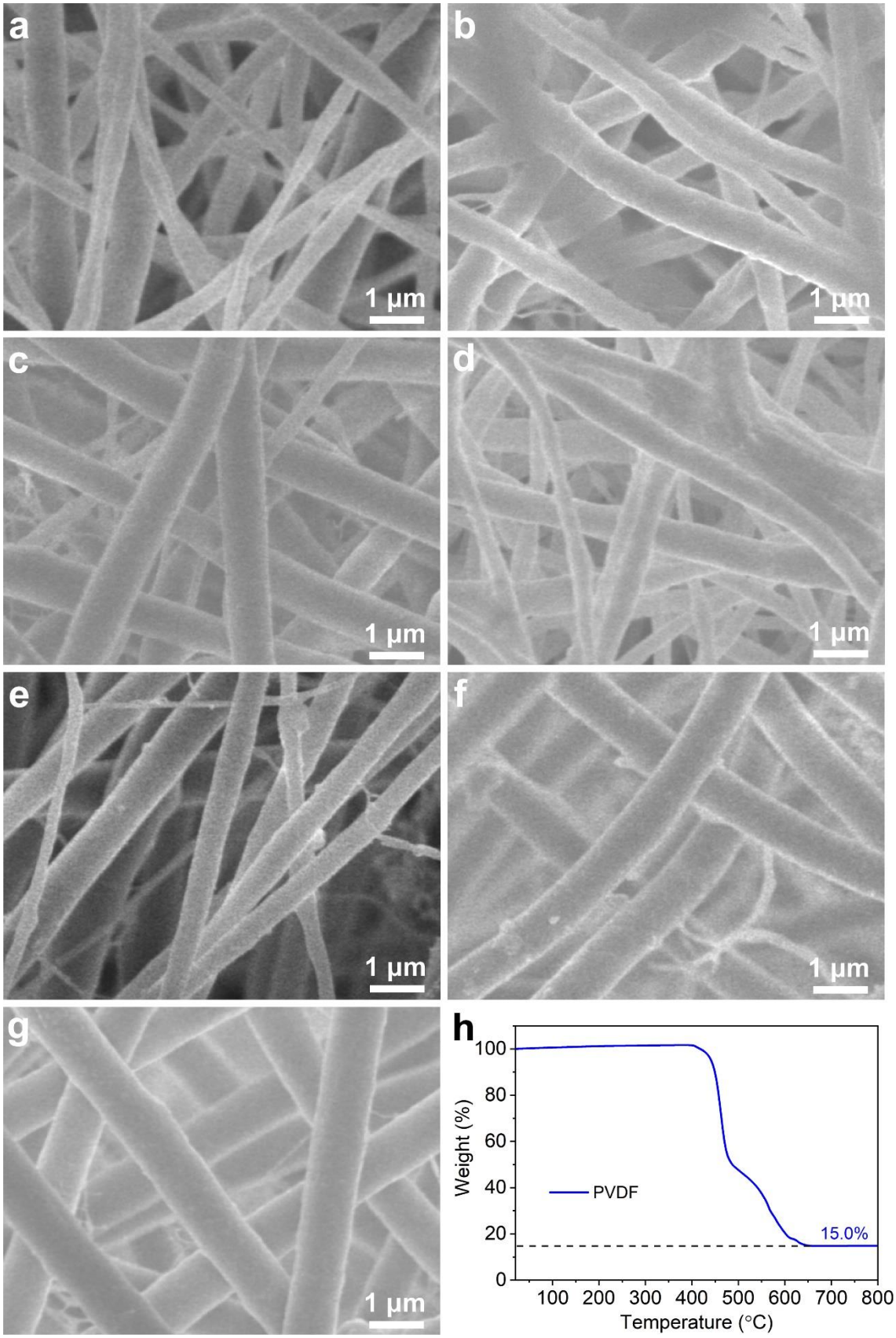

Fig. S1 (a–g) SEM images of KAc/M(Ac)$_2$/PVDF nanofibers without carbonization (M = Mg, Mn, Fe, Co, Ni, Zn, and HE component). (h) TGA curve of PVDF in flowing N_2.

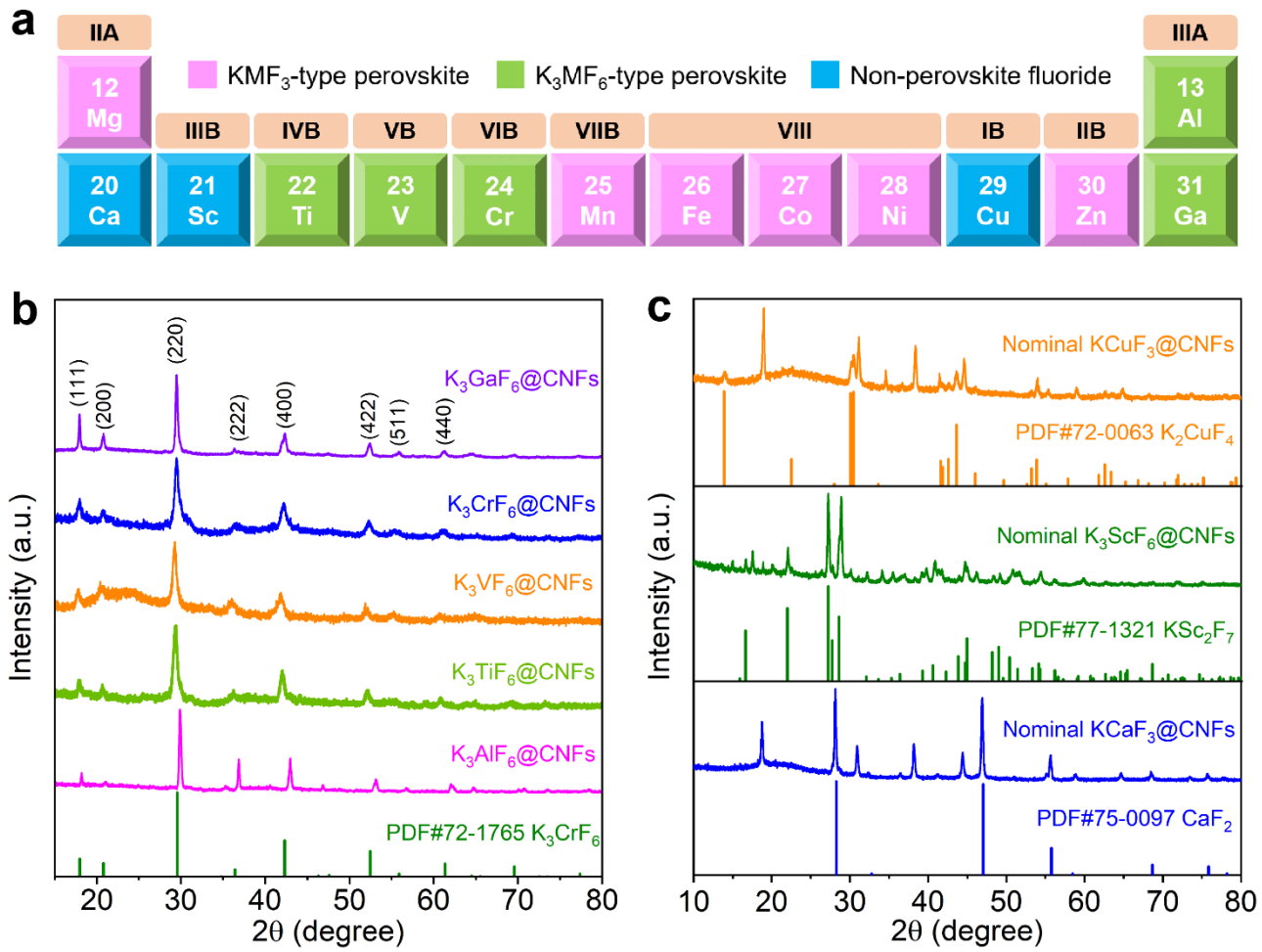

Fig. S2 (a) Schematic representation of the various metal fluorides obtained in this work. XRD patterns of (b) K_3MF_6-type cubic perovskite fluorides and (c) other non-perovskite fluorides.

For trivalent Al, Ti, V, Cr, and Ga, K_3MF_6-type cubic perovskites with the space group $Fm\bar{3}m$ can be obtained, in which one-third of the K atoms occupy the octahedral B site to form $K(K_{0.5}M_{0.5})F_3$ (i.e., K_3MF_6).

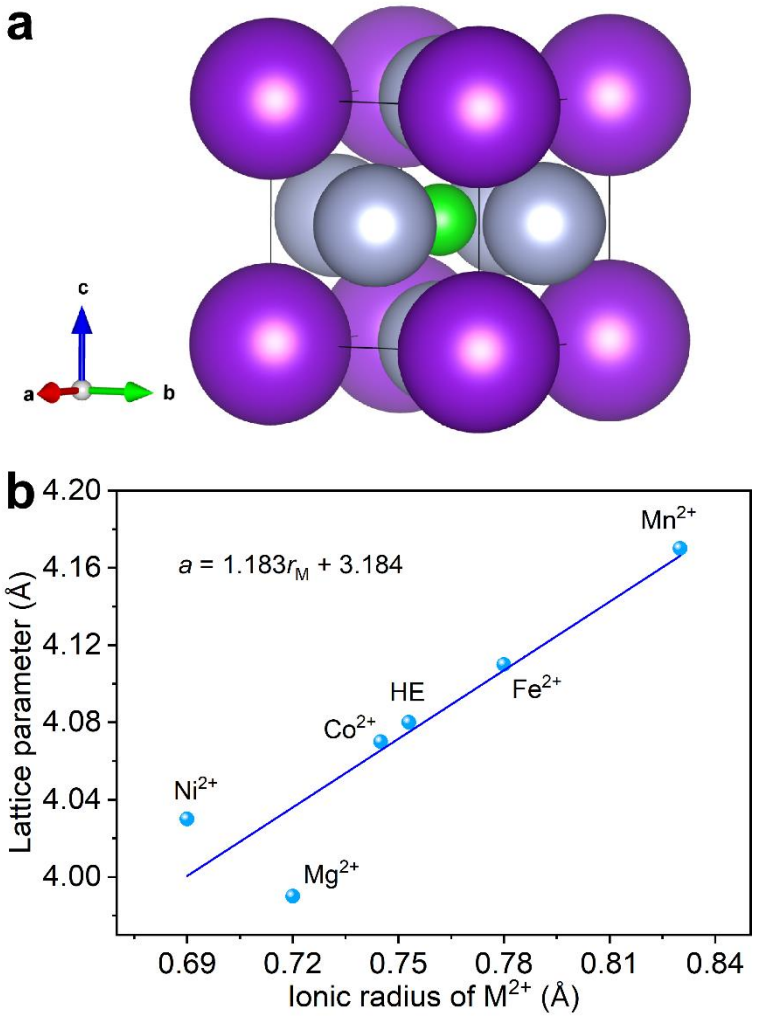

Fig. S3 (a) Space-filling model of KMF_3 perovskite (purple, green, and gray balls represent K, M, and F ions, respectively). (b) Liner fitting between KMF_3@CNFs lattice parameter (a) and six-coordinated M^{2+} ionic radius (r_M).

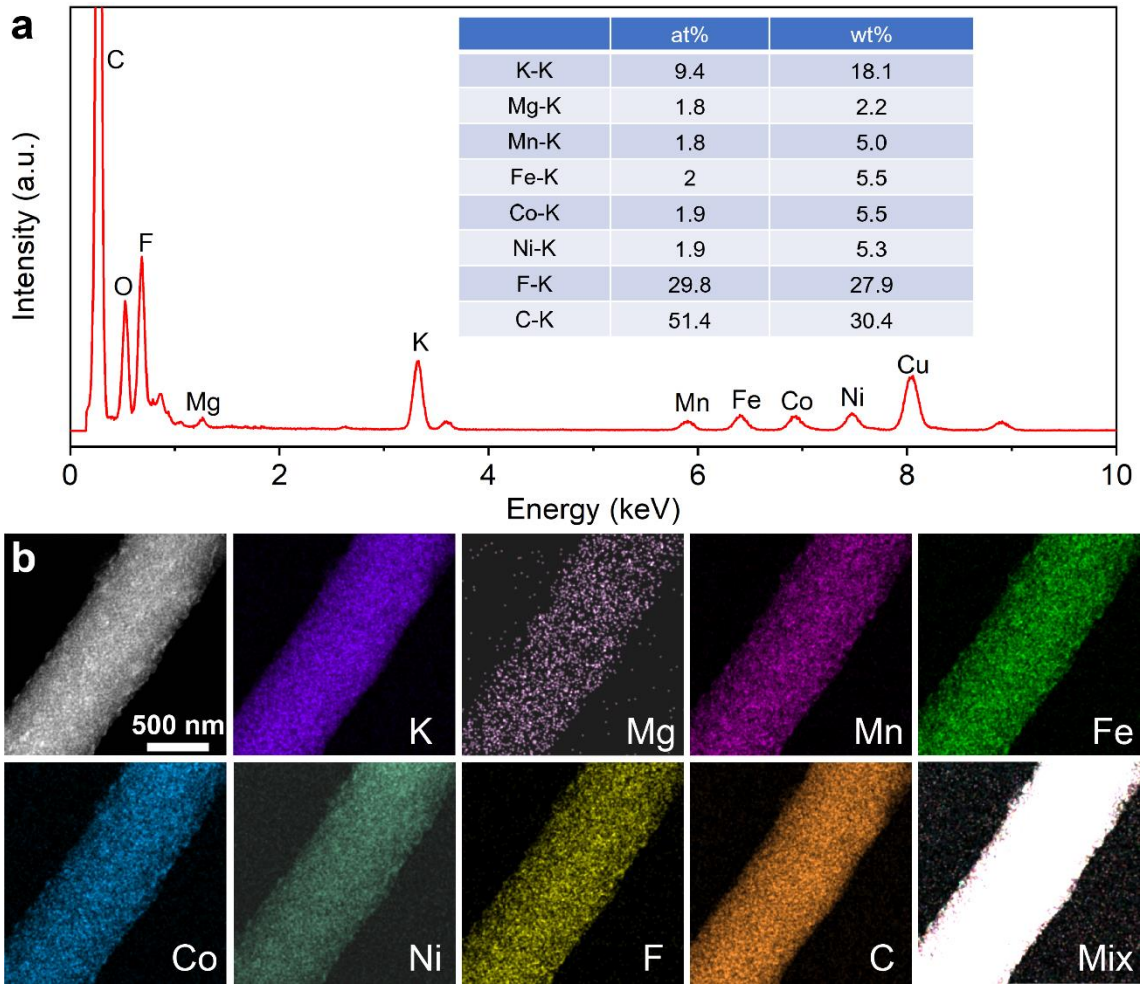

	at%	wt%
K-K	9.4	18.1
Mg-K	1.8	2.2
Mn-K	1.8	5.0
Fe-K	2	5.5
Co-K	1.9	5.5
Ni-K	1.9	5.3
F-K	29.8	27.9
C-K	51.4	30.4

Fig. S4 (a) EDX spectrum of HE-KMF_3@CNFs. (b) Elemental mapping of a single HE-KMF_3@CNF.

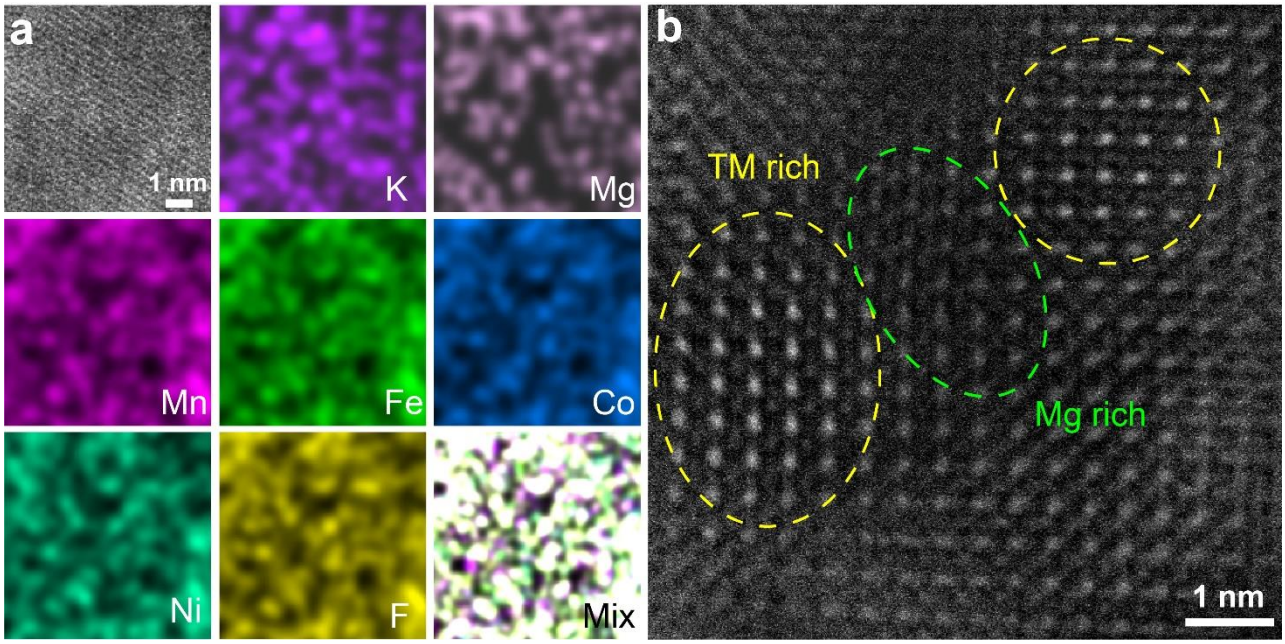

Fig. S5 (a) Atomic-scale elemental mapping and (b) HAADF-STEM image of one HE-KMF_3 particle in HE-KMF_3@CNFs.

As depicted in Fig. 5b, some separated bright-dot and dark-dot regions are observed, indicating the formation of transition metal (TM)-rich and Mg-rich regions, respectively.

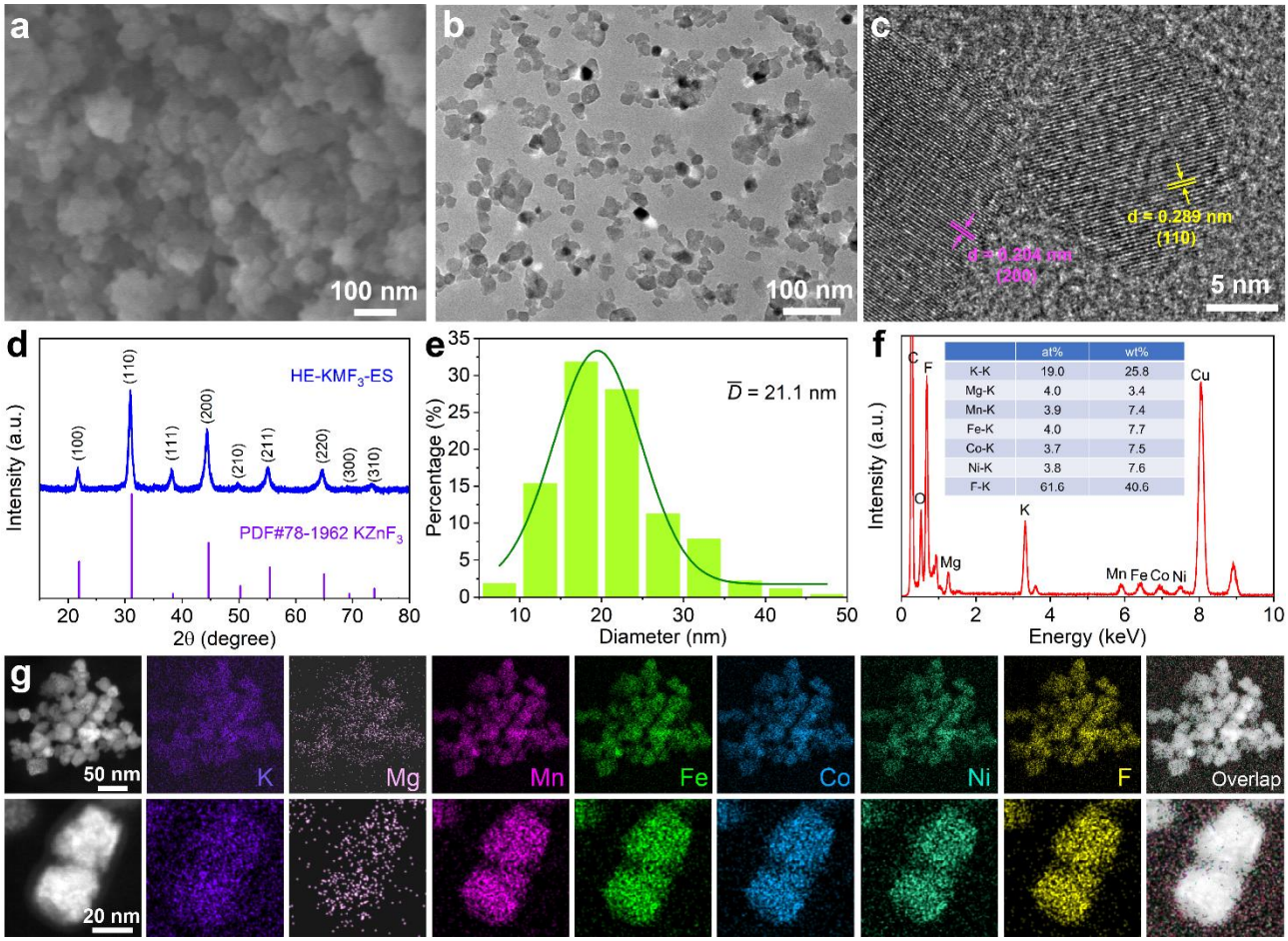

Fig. S6 (a) SEM image, (b) TEM image, (c) HRTEM image, (d) XRD pattern, (e) size distribution, (f) EDX spectrum, and (g) elemental mapping of HE-KMF_3-ES.

After carbon combustion, the average particle size of HE-KMF_3-ES was 21.1 nm (Fig. S6e). The elemental mappings revealed that K, Mg, Mn, Fe, Co, Ni, and F were uniformly distributed throughout the nanoparticles, both at low and high magnifications (Fig. S6g).

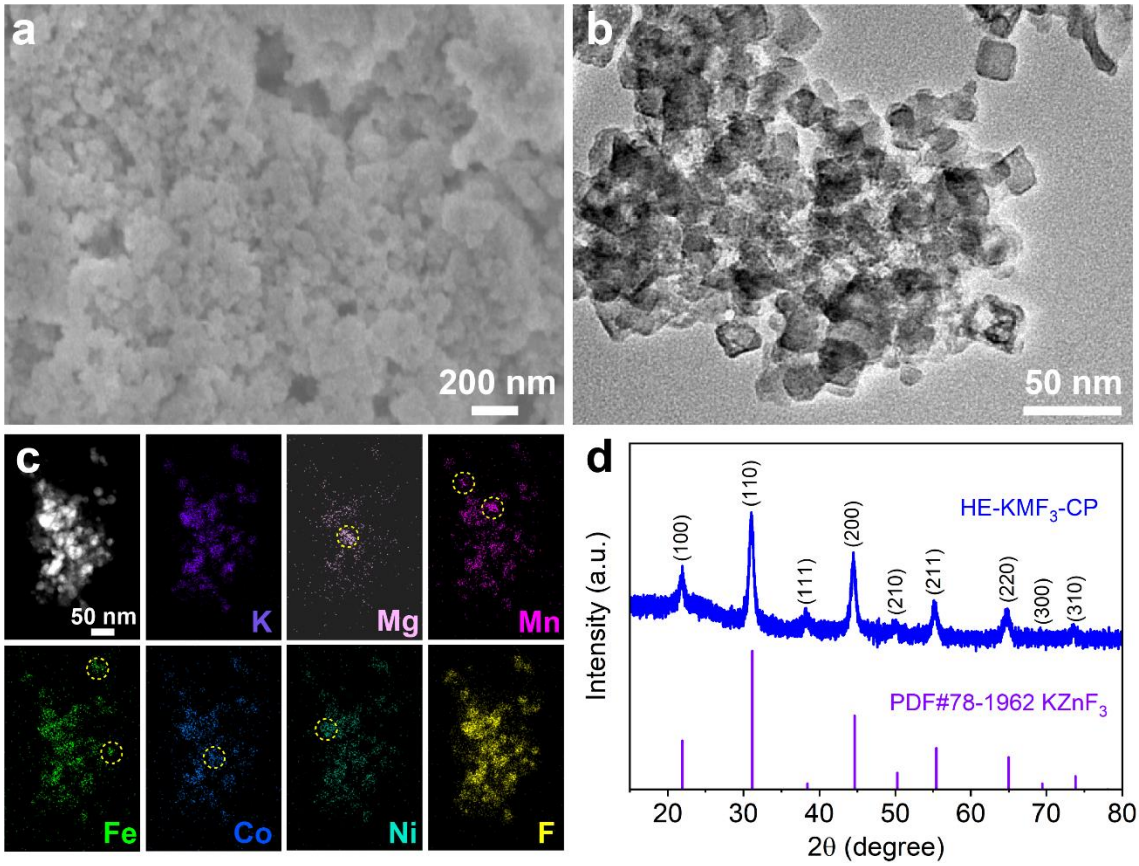

Fig. S7 (a) SEM image, (b) TEM image, (c) elemental mapping, and (d) XRD pattern of HE-KMF_3-CP.

As shown in Fig. S7c, Mg, Mn, Fe, Co, and Ni were unevenly distributed in HE-KMF_3-CP (marked with yellow circles), indicating that the nominal HE material may be a mixture of single-metal fluorides, bimetallic fluorides, or multicomponent fluorides.

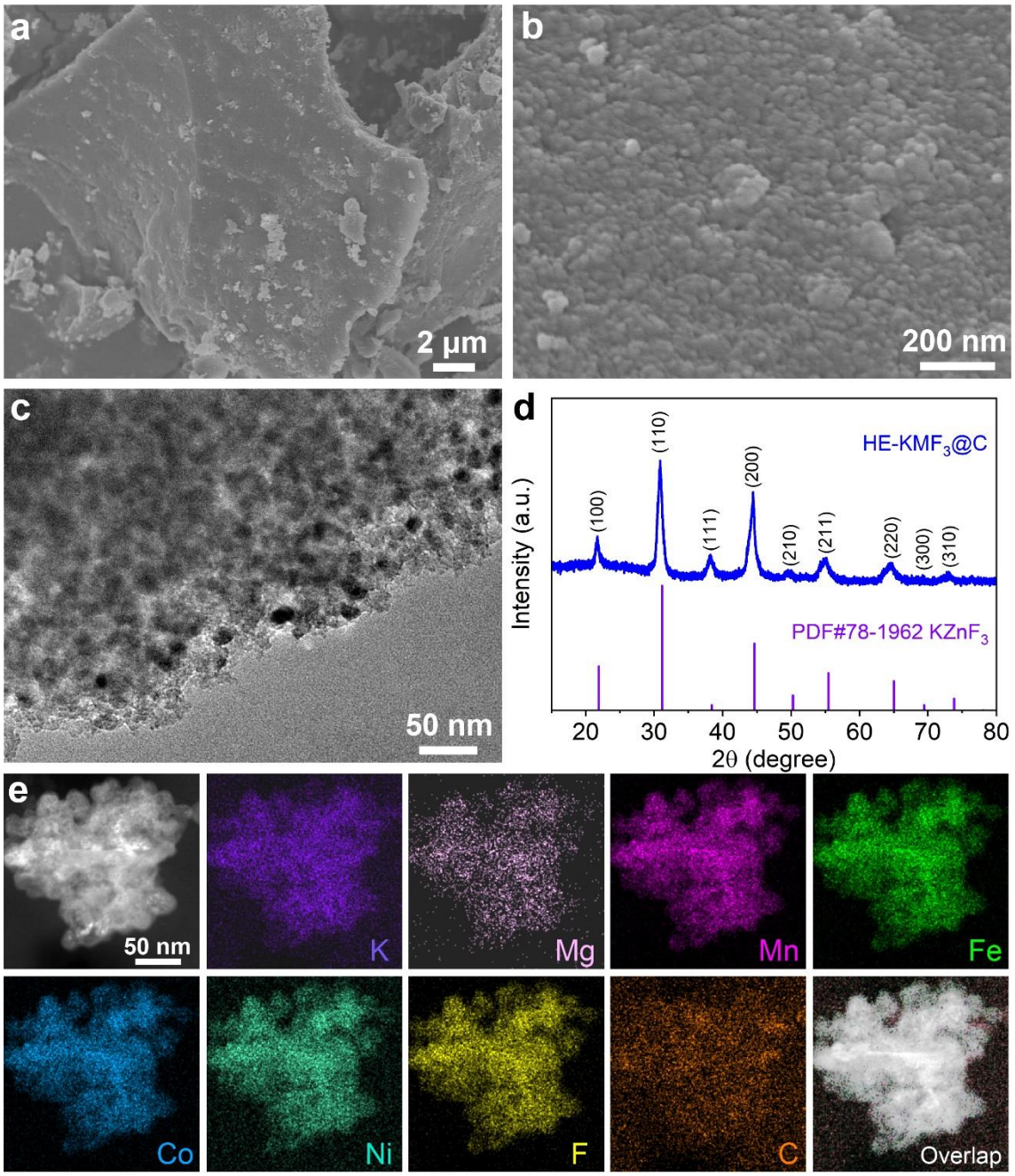

Fig. S8 (a, b) SEM images, (b) TEM image, (d) XRD pattern, and (e) elemental mapping of HE-KMF_3@C.

As displayed in Fig. S8, HE-KMF_3@C consisted of micro-sized irregular particles, with ultrasmall KMF_3 nanoparticles embedded in the carbon matrix. Elemental mappings indicated that K, Mg, Mn, Fe, Co, Ni, F and C were homogeneously distributed in the nanoparticles.

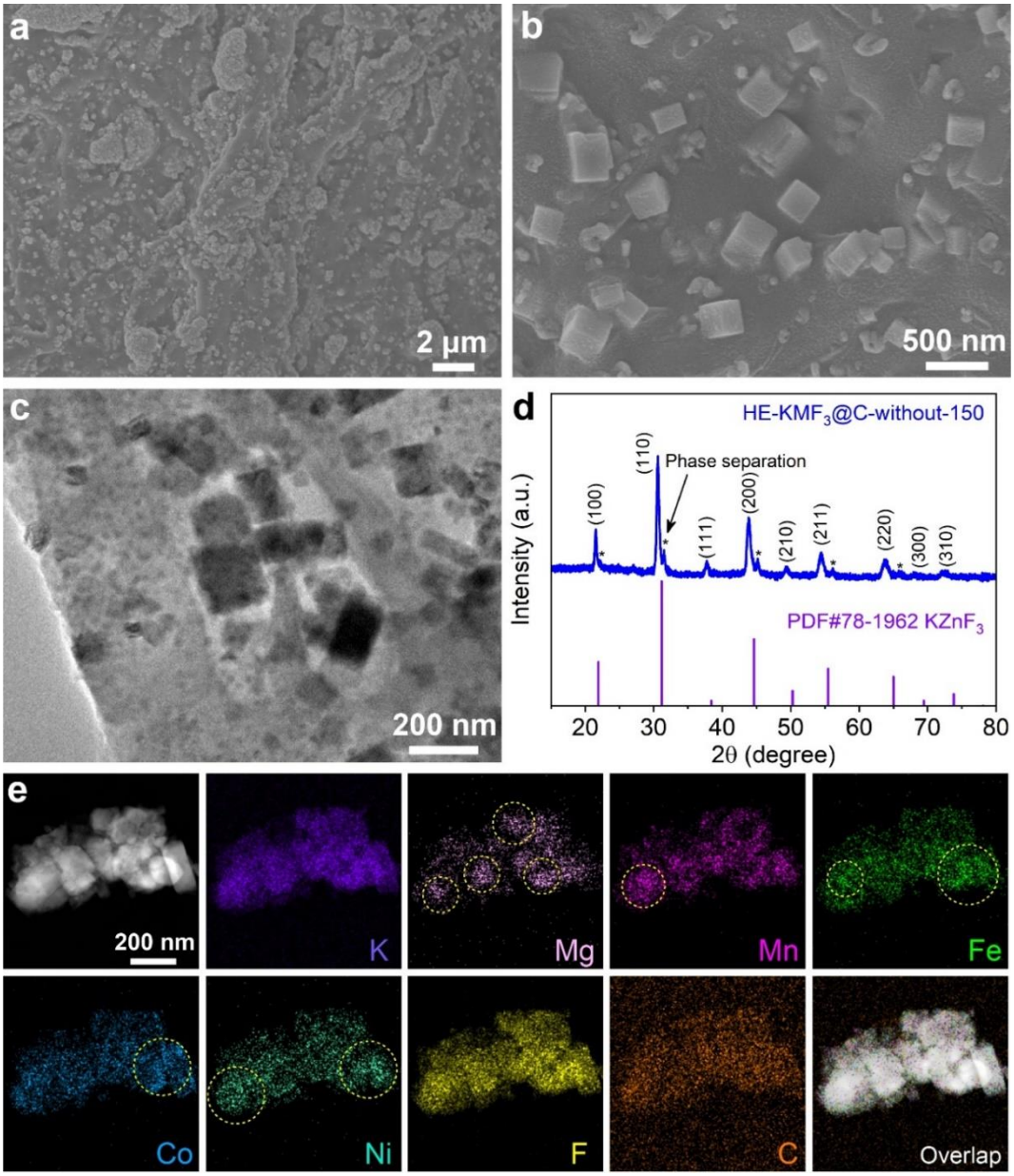

Fig. S9 (a, b) SEM images, (b) TEM image, (d) XRD pattern, and (e) elemental mapping of HE-KMF_3@CNFs synthesized without pretreatment at 150 °C for 1 h (denoted HE-KMF_3@C-without-150).

As illustrated in Fig. S9a and b, the carbon nanofiber structure was destroyed and the KMF_3 particles took on a cubic morphology with particle sizes of 100–400 nm, suggesting that the {100} facets were exposed. Elemental mapping showed that Mg, Mn, Fe, Co, and Ni were unevenly distributed in HE-KMF_3@C-without-150. XRD pattern also revealed the presence of phase separation. These indicate that HE-KMF_3@C-without-150 is also a nominal HE material.

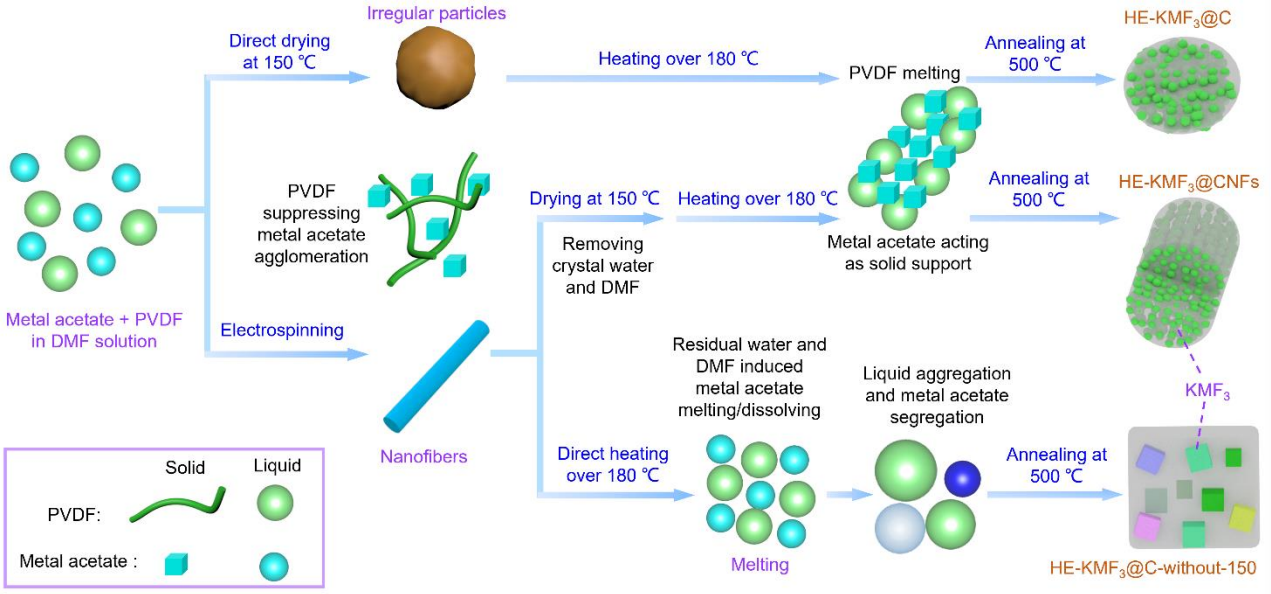

Fig. S10 Schematic illustration of the synthesis and formation mechanisms of HE-KMF_3@C, HE-KMF_3@CNFs, and HE-KMF_3@C-without-150.

i) During the drying and electrospinning processes, the polymer PVDF can effectively inhibit the agglomeration of metal acetate and the segregation of different metal ions.

ii) Without pretreatment at 150 ℃, the residual water and DMF in the electrospun film will cause the melting or dissolution of metal acetate during heating process. For example, the melting point of $Mn(Ac)_2{\cdot}4H_2O$ is only 80 ℃. When the temperature rises beyond the melting point of PVDF (170~180 ℃), the electrospun membrane loses its solid support, leading to the destruction of the nanofiber structure, agglomeration of metal acetate, and segregation of five metal ions (for HE-KMF_3@C-without-150 sample). In contrast, pretreatment at 150 ℃ can remove the crystal water and DMF without melting PVDF. Solid metal acetates in HE-KMF_3@C and HE-KMF_3@CNFs can serve as supports to maintain their original structures after PVDF is melted.

iii) The aggregation of metal acetate in HE-KMF_3@C-without-150 causes the KMF_3 particle size to increase during the annealing process and results in an inhomogeneous carbon coating on the exposed {100} faces of KMF_3 due to their lowest surface energy.

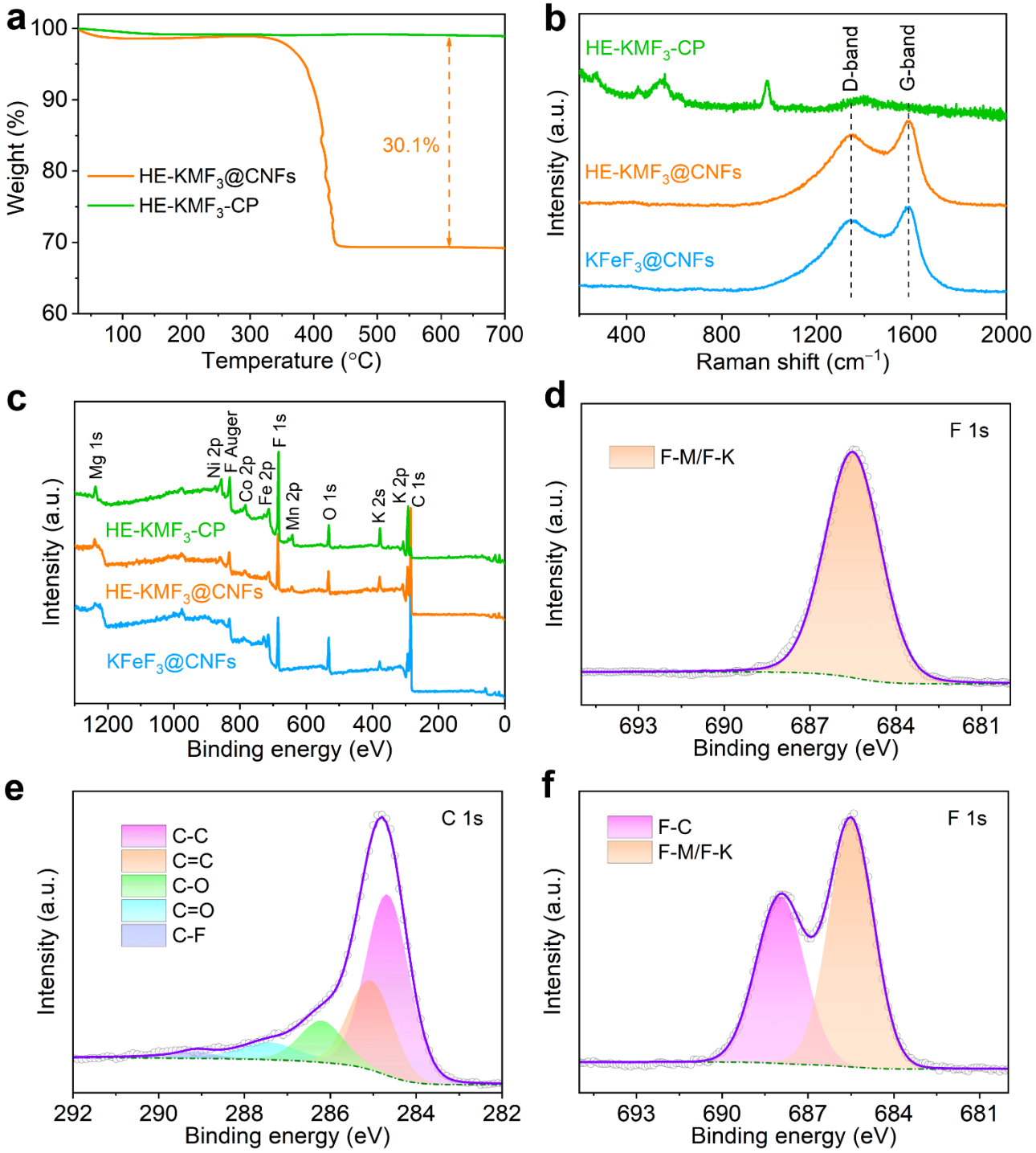

Fig. S11 (a) TGA profiles of HE-KMF_3@CNFs and HE-KMF_3-CP in air. (b) Raman spectra and (c) XPS spectra of $KFeF_3$@CNFs, HE-KMF_3@CNFs, and HE-KMF_3-CP. (d) High-resolution F 1s XPS spectrum of HE-KMF_3-CP. (e) High-resolution C 1s XPS spectrum and (f) high-resolution F 1s XPS spectrum of HE-KMF_3@CNFs.

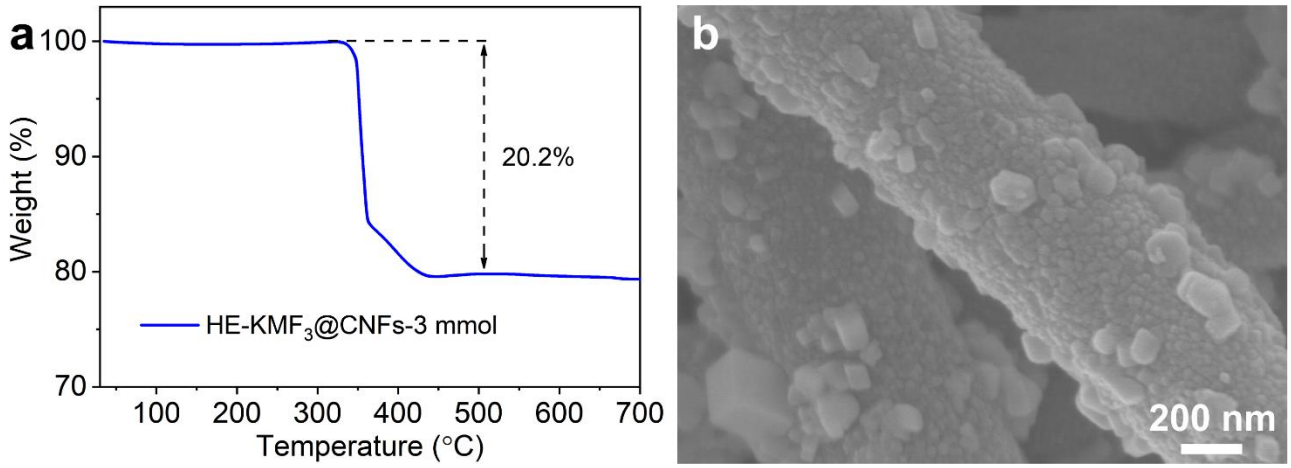

Fig. S12 (a) TGA curve in air and (b) SEM image of HE-KMF_3@CNFs-3 mmol. Note that KMF_3@CNFs-3 mmol was prepared under the same conditions as HE-KMF_3@CNFs, except that the amount of metal acetate $M(Ac)_2 \cdot xH_2O$ was increased from 2 mmol to 3 mmol.

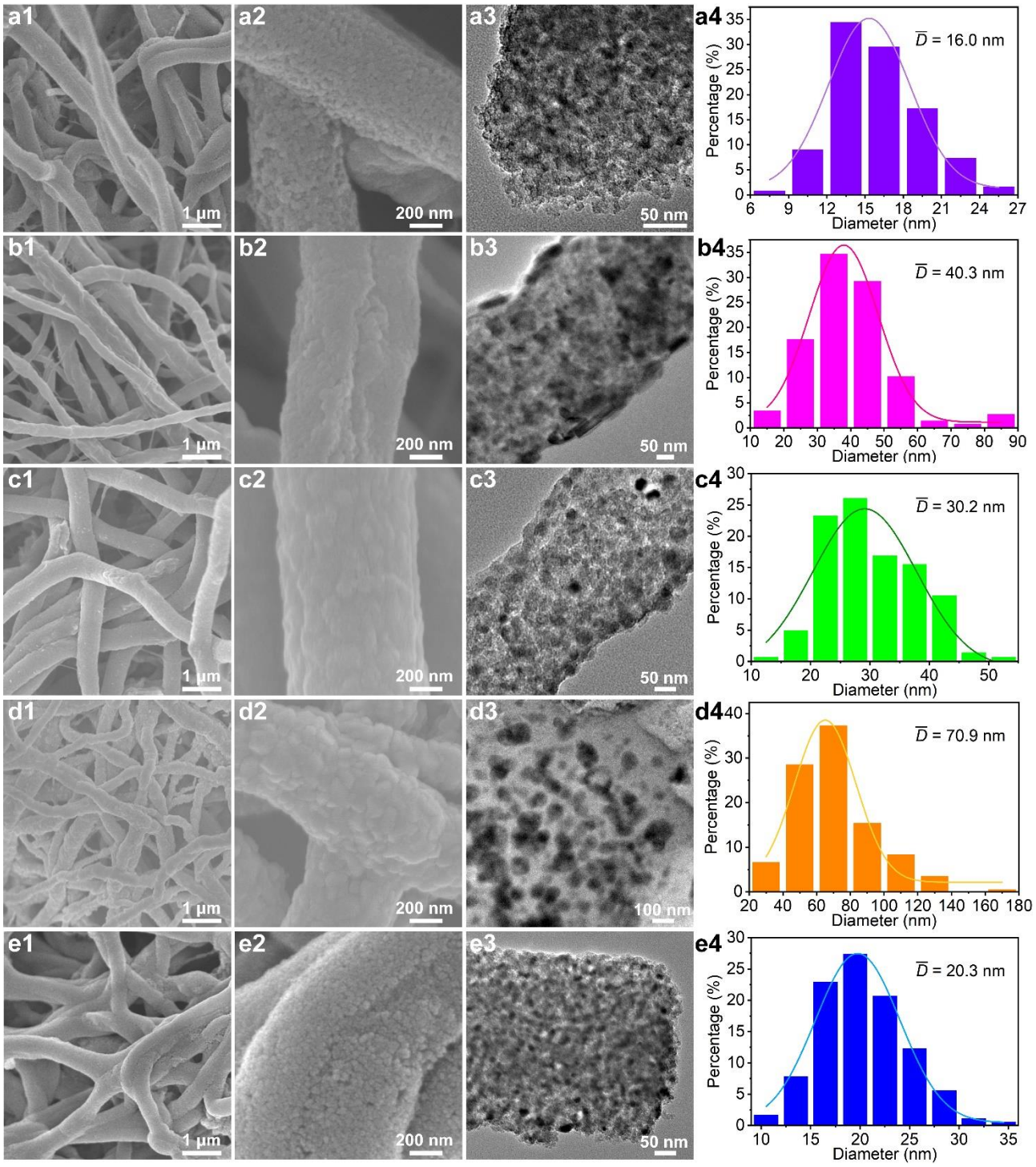

Fig. S13 SEM images, TEM image, and size distribution of KMF_3@CNFs, M = (a) Mg, (b) Mn, (c) Fe, (d) Co, and (e) Ni.

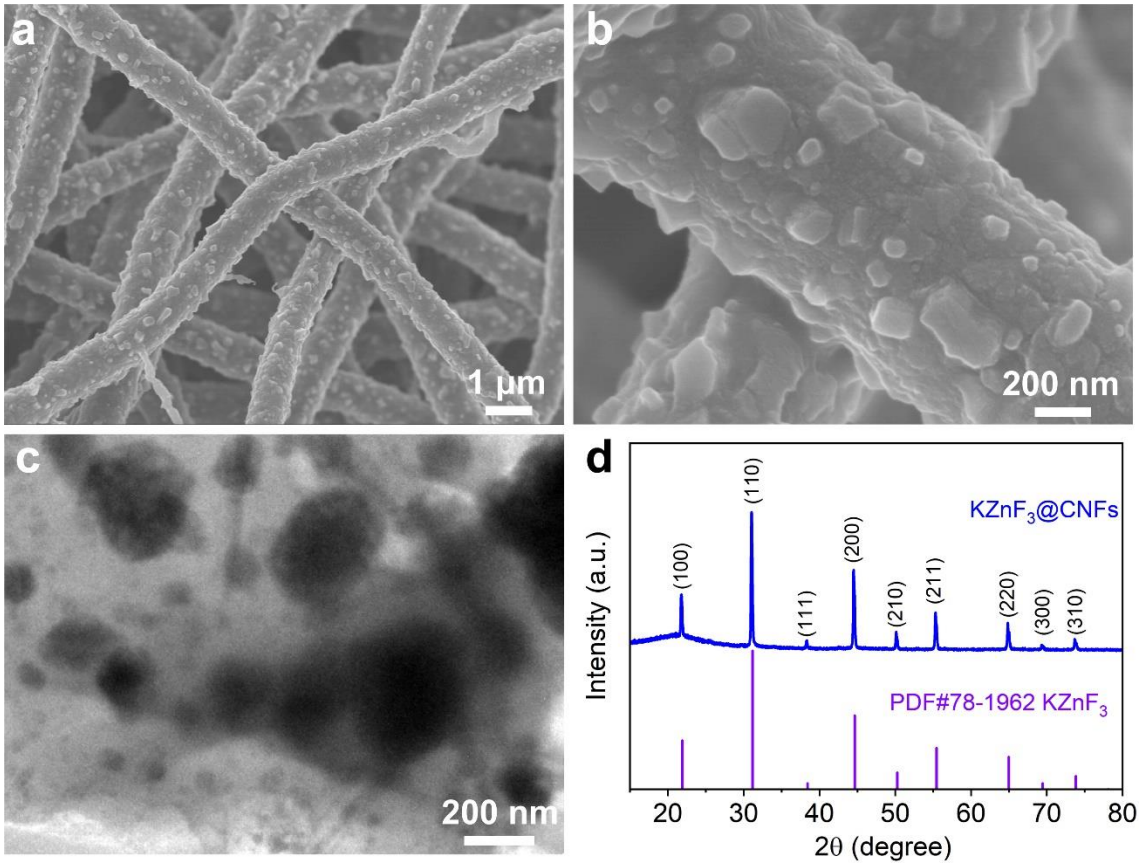

Fig. S14 (a, b) SEM images, (c) TEM image, and (d) XRD pattern of $KZnF_3$@CNFs.

Unlike other KMF_3@CNFs in Fig. S13, $KZnF_3$ nanoparticles appear on the surface of CNFs, and the size of several particles increases to ~200 nm. This may be due to the low boiling point of ZnO, which evaporates and aggregates during pyrolysis.

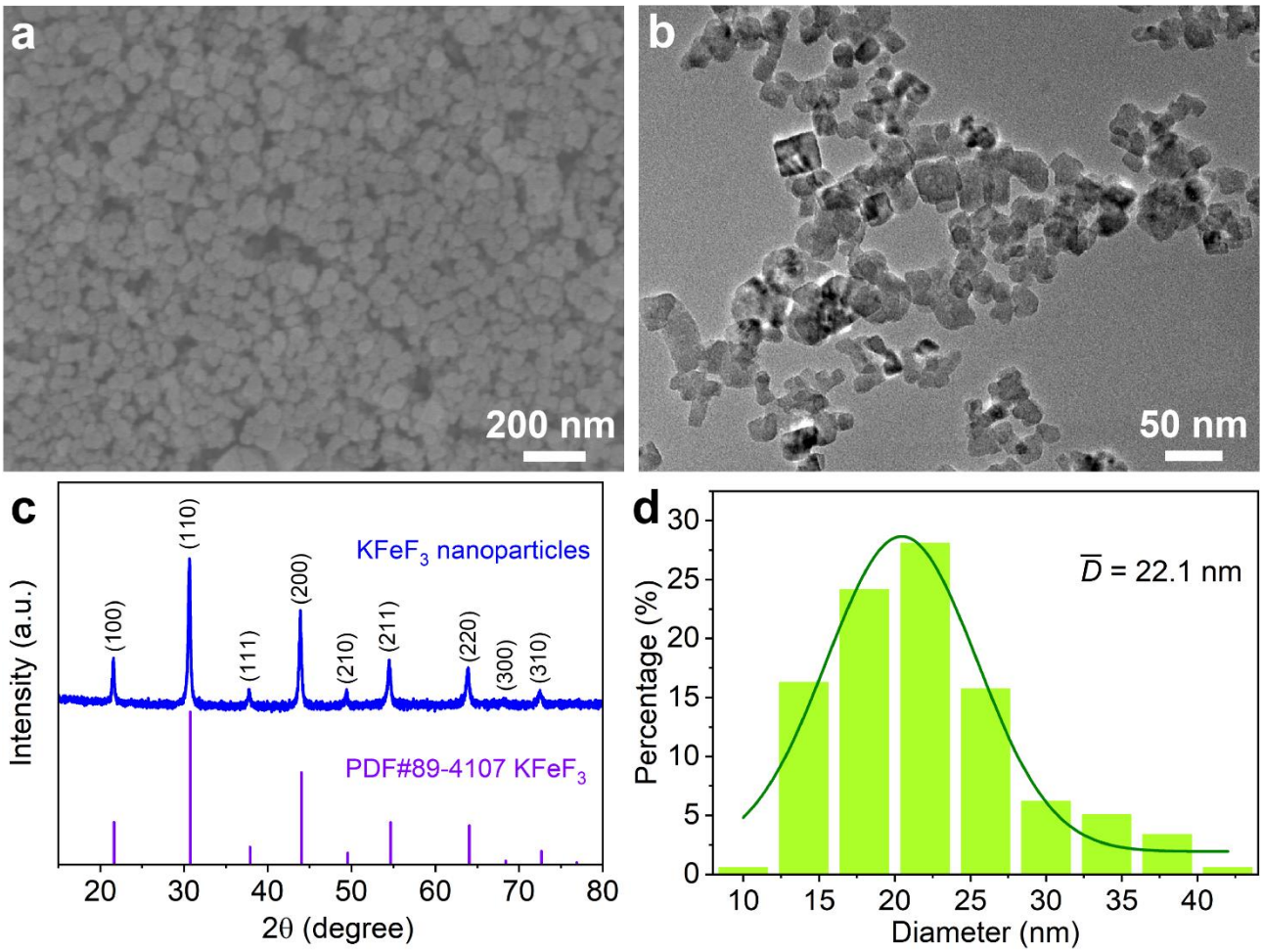

Fig. S15 (a) SEM image, (b) TEM image, (c) XRD pattern, and (d) size distribution of $KFeF_3$ nanoparticles obtained by solvothermal method.

The average particle size of the solvothermal synthesized $KFeF_3$ nanoparticles is 22.1 nm, which is close to HE-KMF_3-ES (21.1 nm, see Fig. S6) and is suitable for subsequent electronic conductivity comparison.

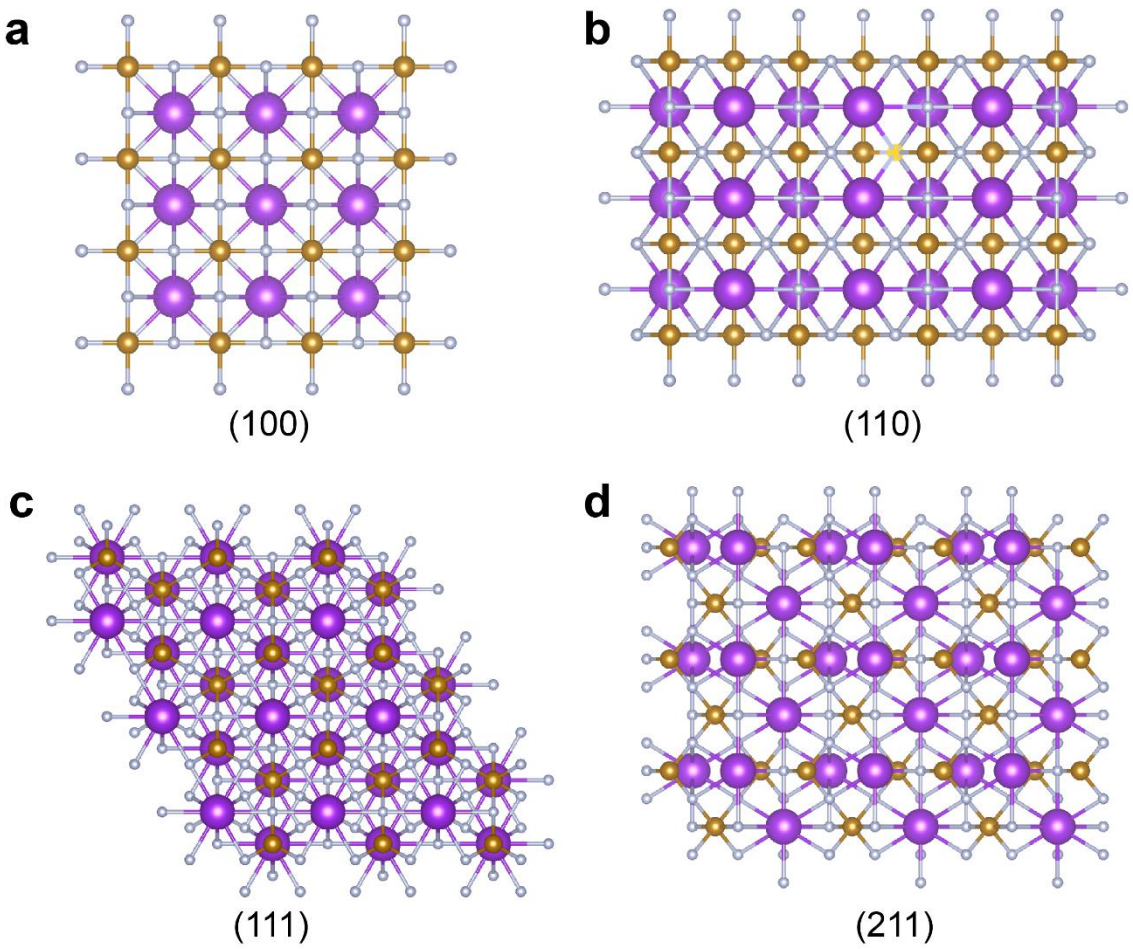

Fig. S16 Different exposed surfaces of $KFeF_3$: (a) (100), (b) (110), (c) (111), and (d) (211).

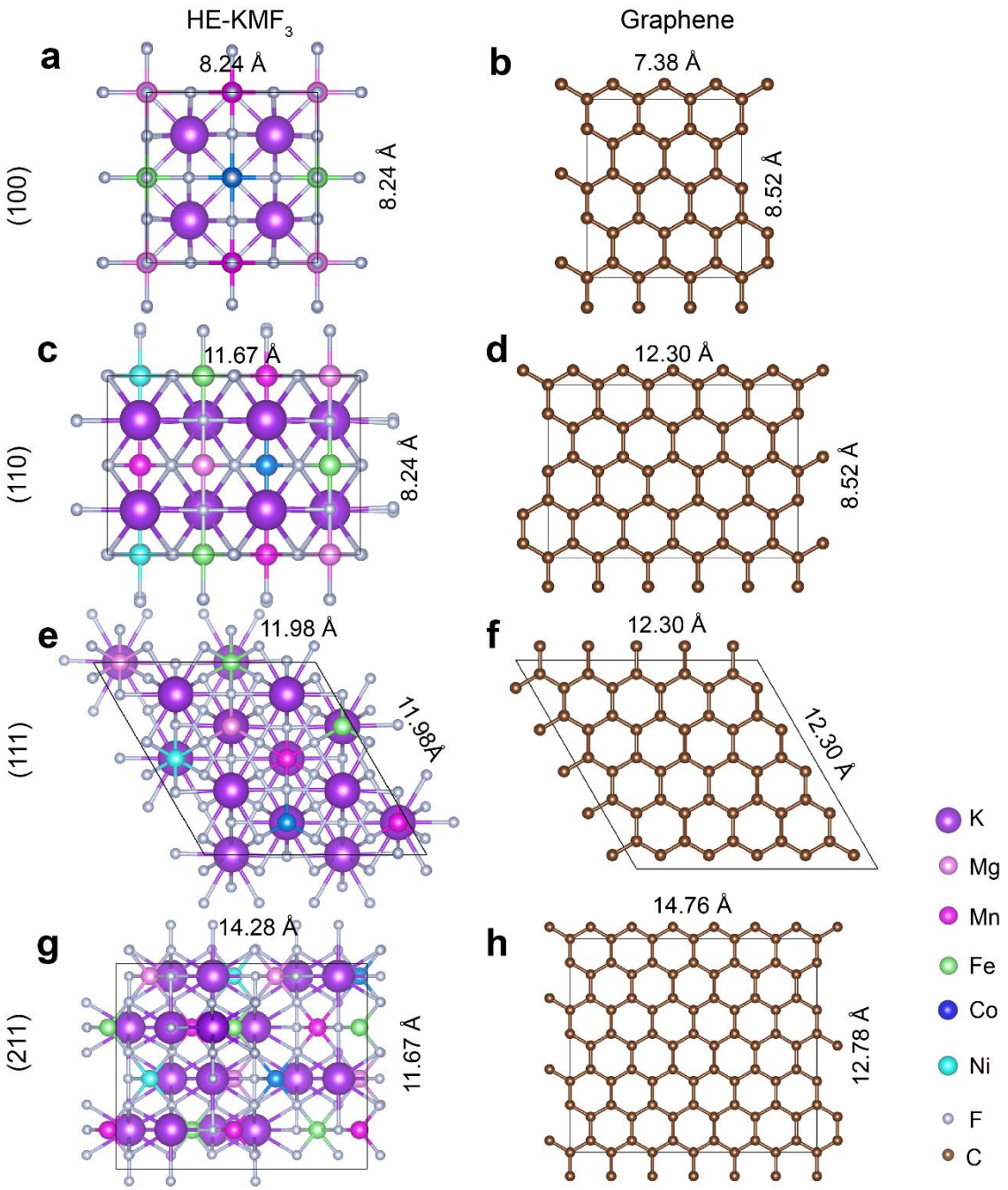

Fig. S17 Superlattice constructed with different surfaces of HE-KMF_3 and graphene: (a, b) (100) plane, (c, d) (110) plane, (e, f) (111) plane, and (g, h) (211) plane.

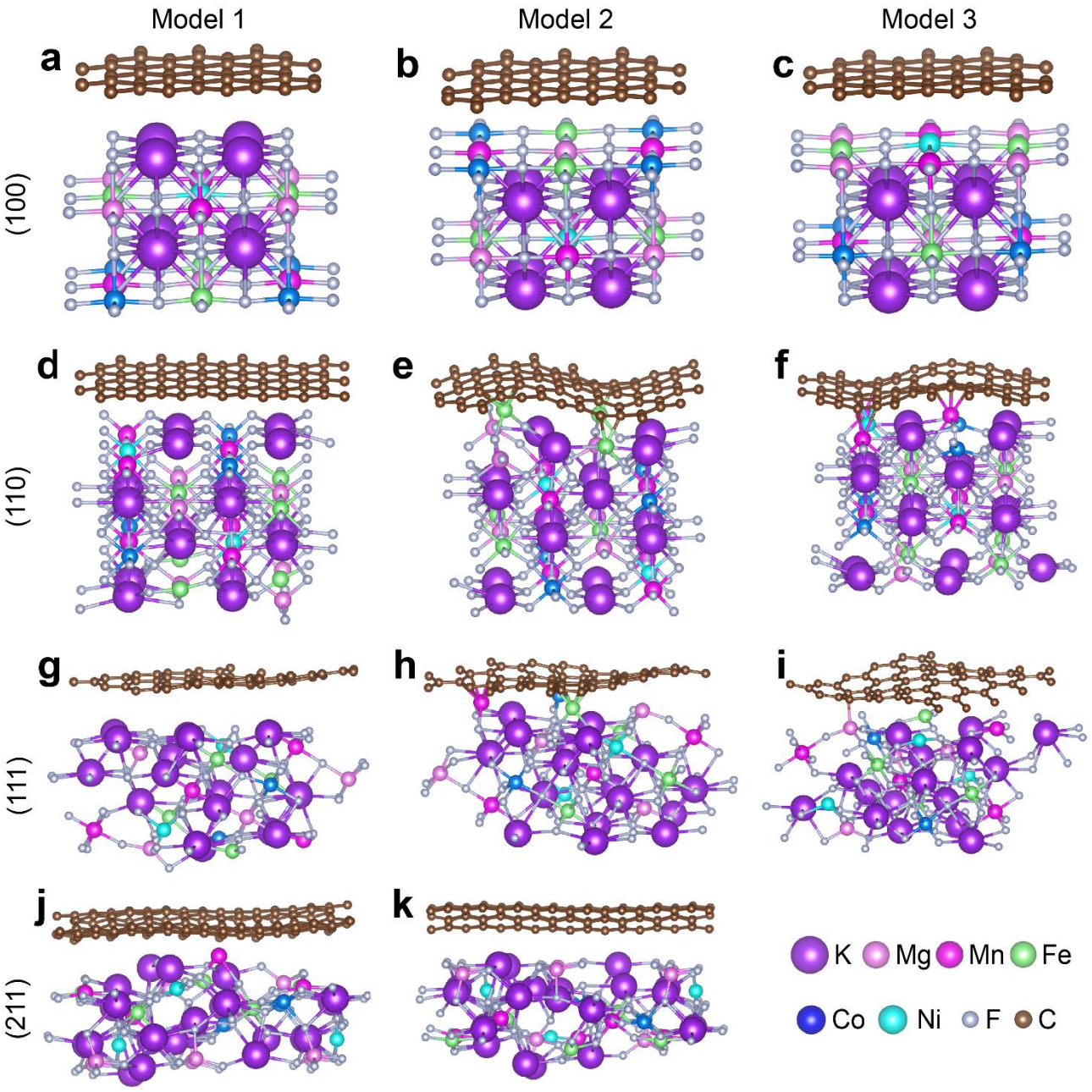

Fig. S18 Optimized models for graphene adsorption on different surfaces of HE-KMF_3: (a–c) (100) plane, (d–f) (110) plane, (g–i) (111) plane, and (j, k) (211) plane.

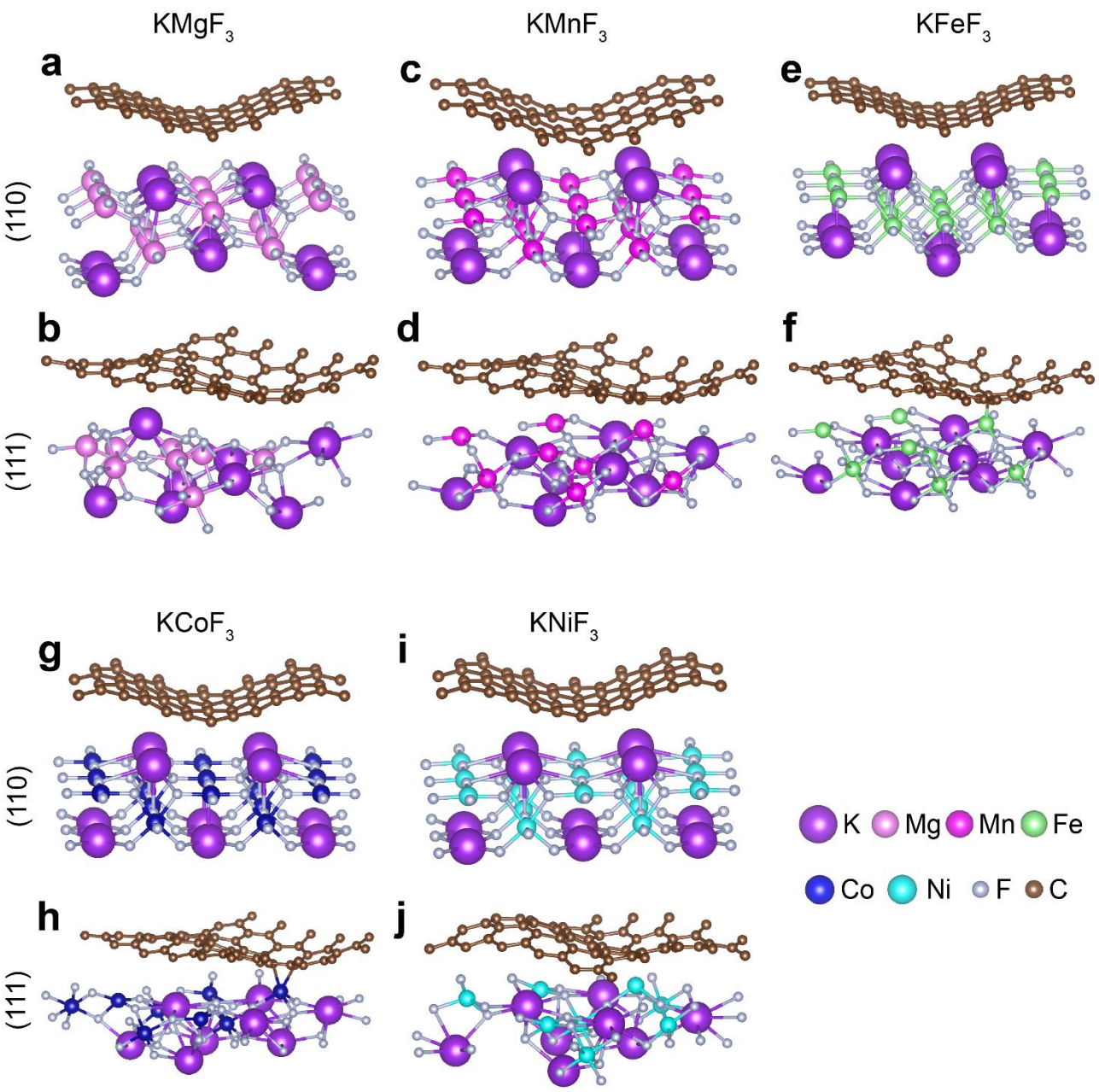

Fig. S19 Optimization models of graphene adsorption on the (110) and (111) surfaces of KMF_3 (M = Mg, Mn, Fe, Co, and Ni): (a, b) Mg, (c, d) Mn, (e, f) Fe, (g, h) Co, and (h, j) Ni.

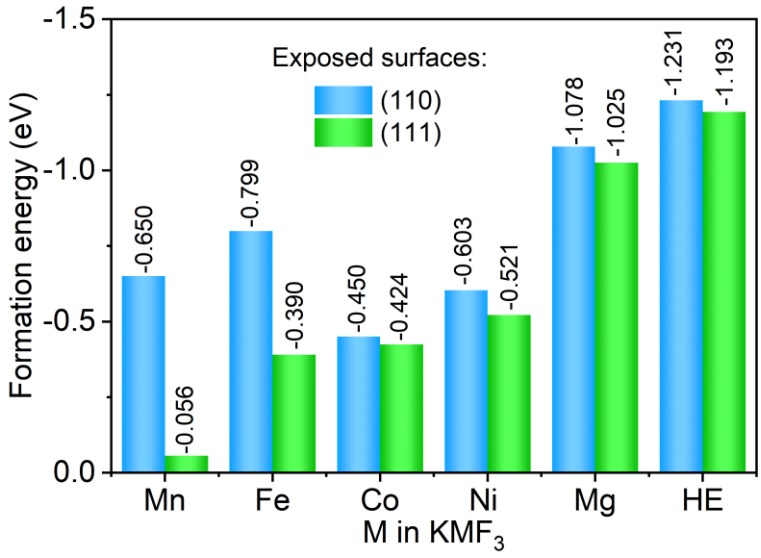

Fig. S20 Calculated formation energies of graphene acting on the (110) or (111) planes of KMF_3 (M = Mg, Mn, Fe, Co, Ni, and HE).

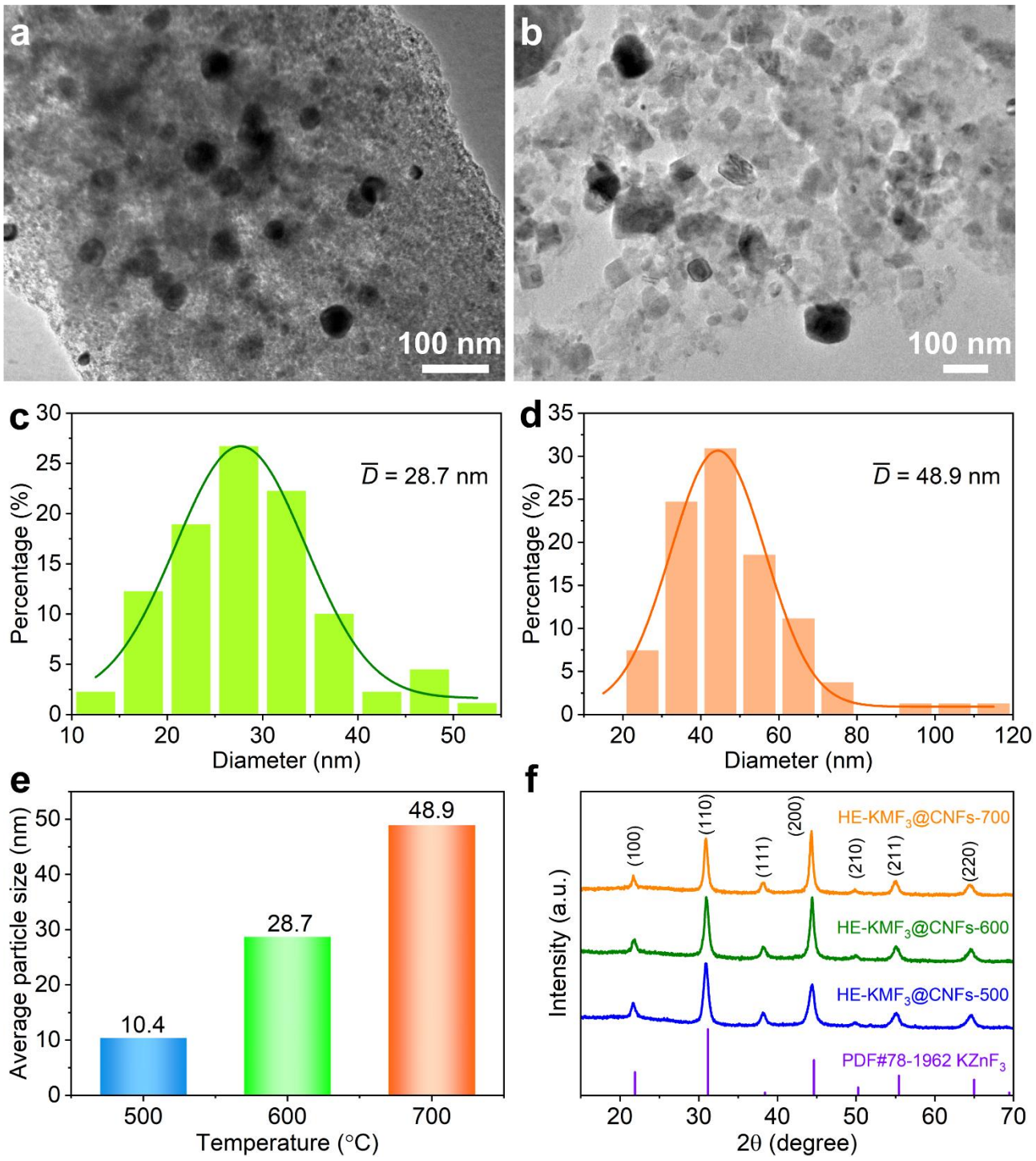

Fig. S21 TEM images and size distribution of HE-KMF_3@CNFs annealed at (a, c) 600 ℃ and (b, d) 700 ℃. (e) Average particle size and (f) XRD patterns of HE-KMF_3@CNFs annealed at different temperatures.

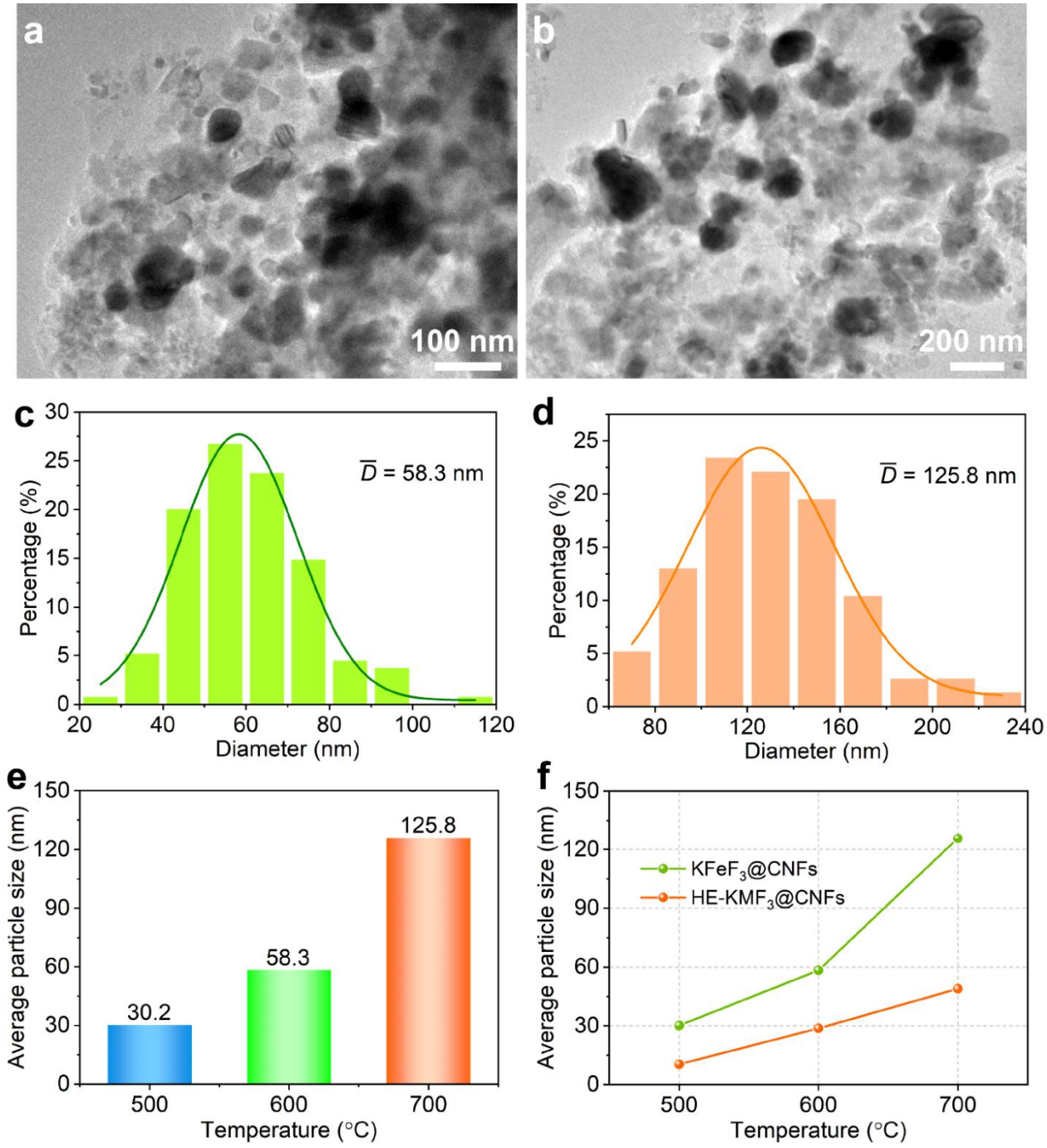

Fig. S22 TEM images and size distribution of $KFeF_3$@CNFs annealed at (a, c) 600 ℃ and (b, d) 700 ℃. (e) Average particle size of $KFeF_3$@CNFs and (f) comparison of particle sizes of $KFeF_3$@CNFs and HE-KMF_3@CNFs at various annealing temperatures.

As the annealing temperature increases, the average particle sizes of HE-KMF_3@CNFs and $KFeF_3$@CNFs increase. However, the growth trend of $KFeF_3$@CNFs is stronger, reflecting that the HE structure can also effectively suppress grain growth even at higher annealing temperature.

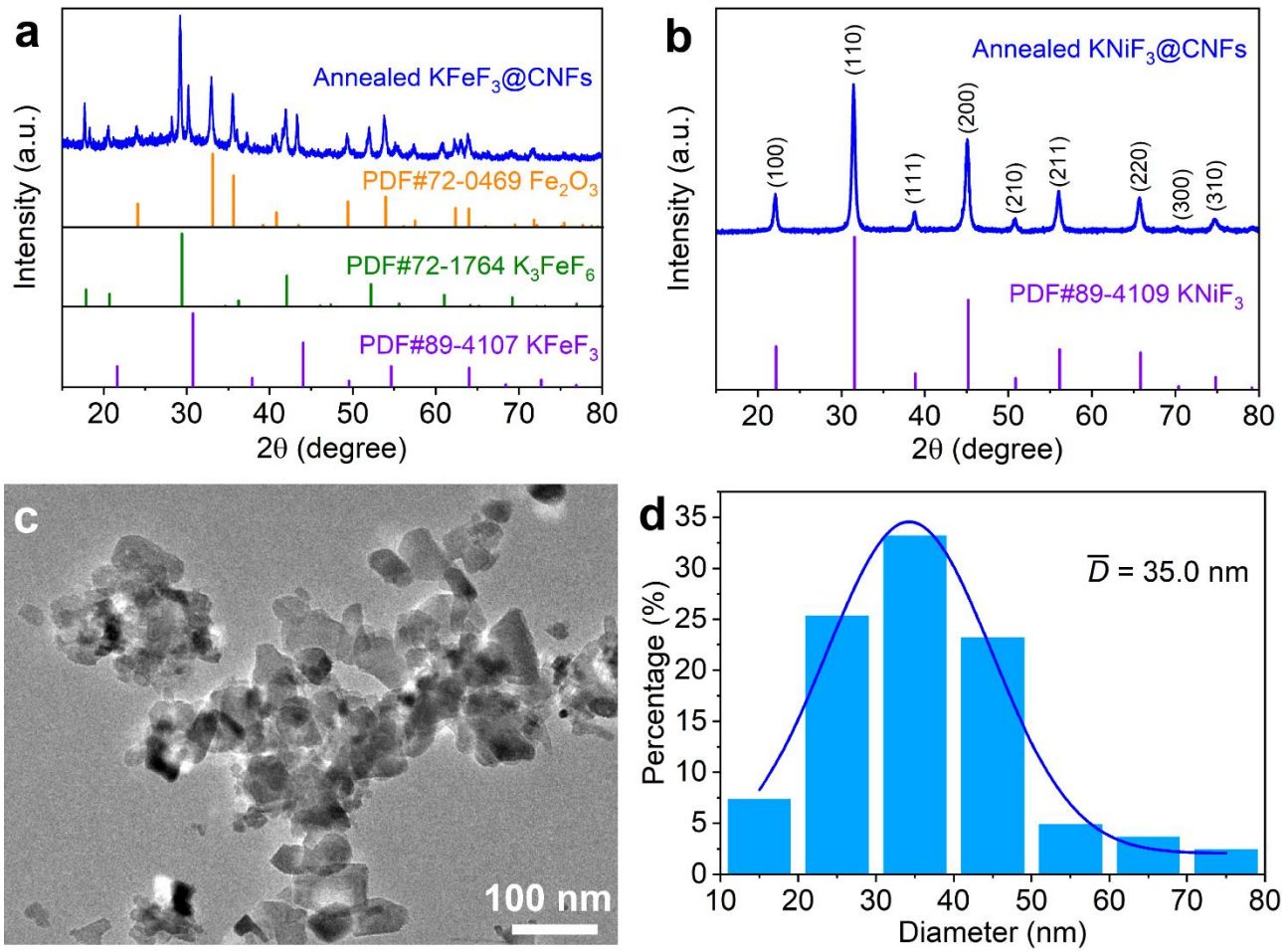

Fig. S23 (a) XRD pattern of $KFeF_3$@CNFs after annealing at 500 ℃ for 1 h in air, (b) XRD pattern, (c) TEM image, and (d) size distribution of $KNiF_3$@CNFs after annealing at 500 ℃ for 1 h in air.

XRD results show that $KFeF_3$ is unstable, while $KNiF_3$ is stable when annealed in air at 500 ℃ (Fig. S23a, b). Therefore, we obtained monometal fluoride $KNiF_3$ from KMF_3@CNFs. After carbon burning, the average particle size of $KNiF_3$ increased from 20.3 nm to 35.0 nm (Fig. S13e and S23c, d).

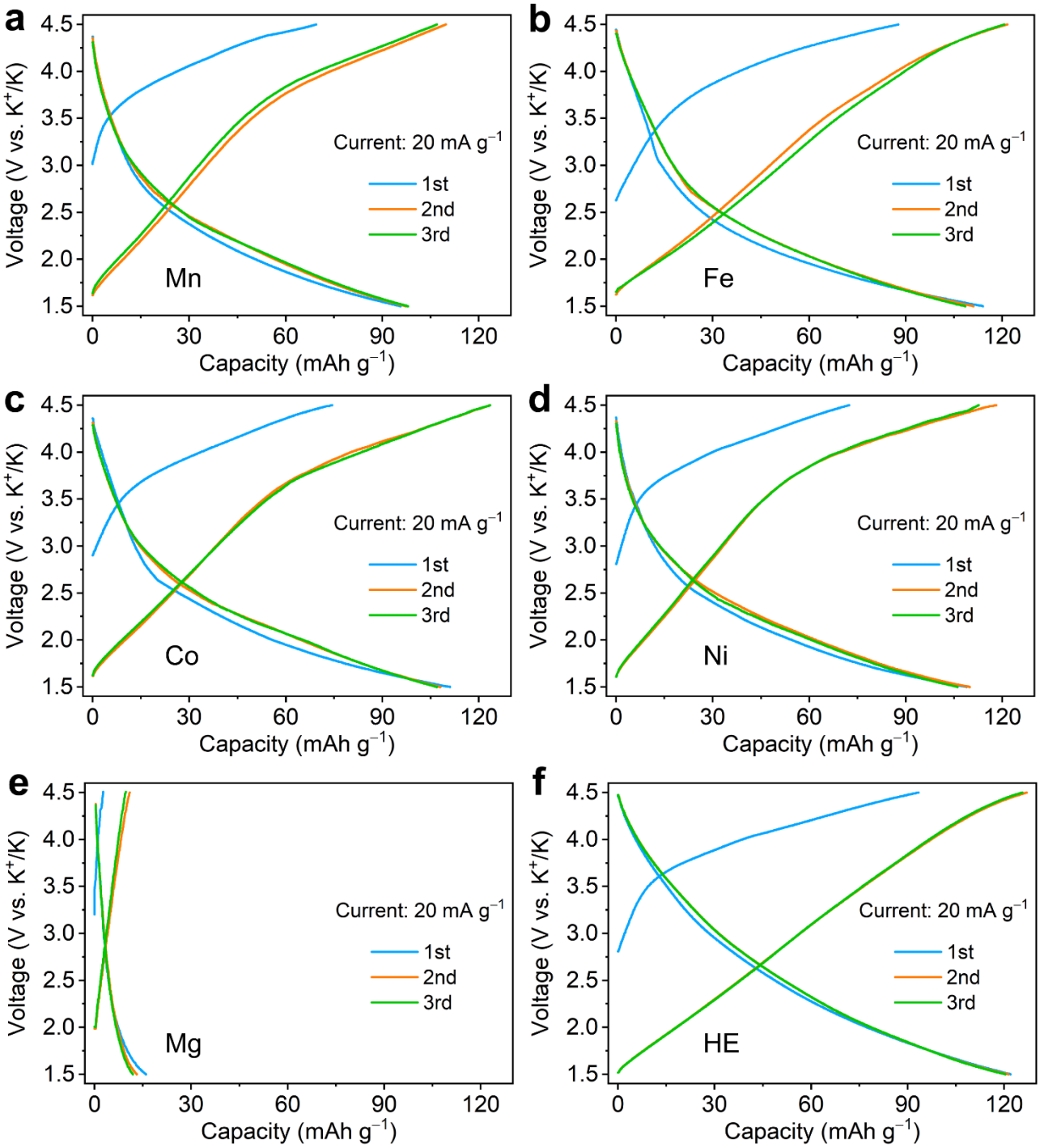

Fig. S24 The initial three charge/discharge curves of KMF_3@CNFs, M = (a) Mn, (b) Fe, (c) Co, (d) Ni, (e) Mg, and (f) HE.

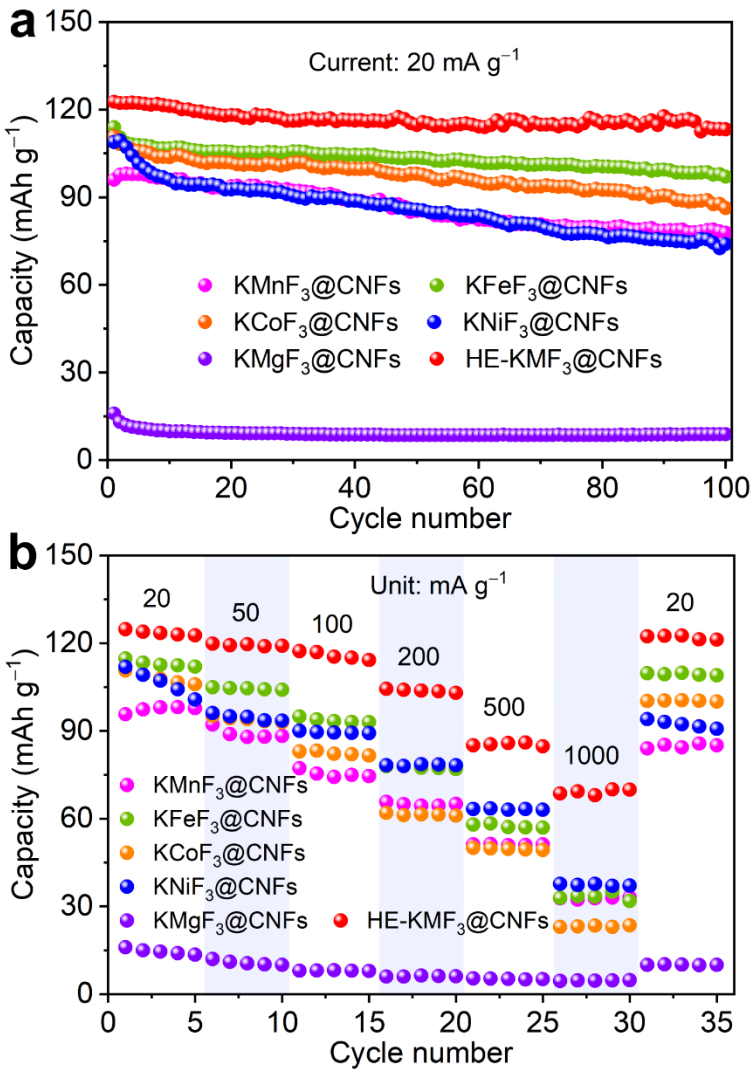

Fig. S25 Electrochemical characterization of KMF_3@CNFs: (a) cycling performances and (b) rate capabilities.

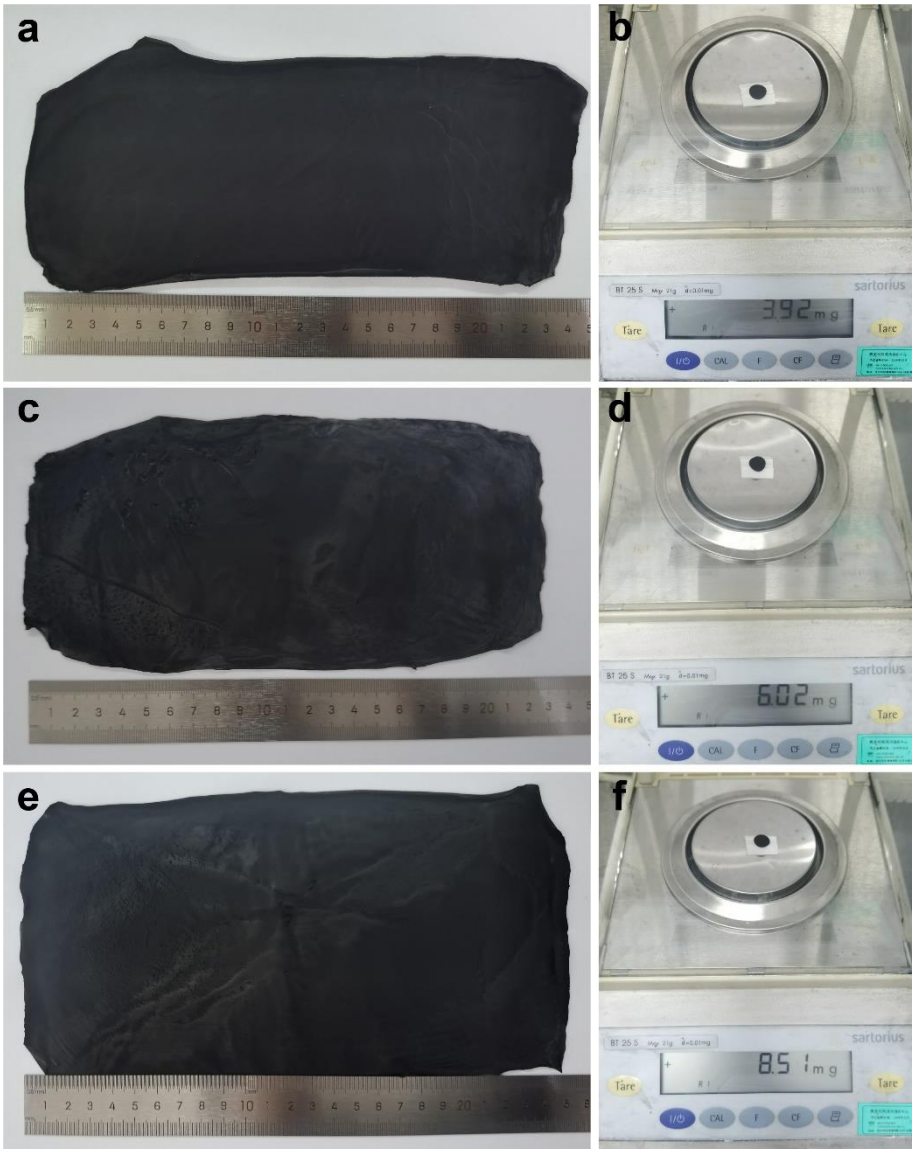

Fig. S26 (a, c, e) Digital images of self-supporting HE-KMF_3@CNFs membranes with different thicknesses and (b, d, f) the corresponding digital images of self-supporting electrodes with a diameter of 10 mm. The mass loading of HE-KMF_3@CNFs for samples (a), (c), and (e) is approximately 5.0, 7.7, and 10.8 mg cm^{-2}, respectively.

It is worth mentioning that the areal capacity of self-supporting HE-KMF_3@CNFs membrane electrodes can reach 1.27 mAh cm^{-2} (see Fig. 3h in the main text).

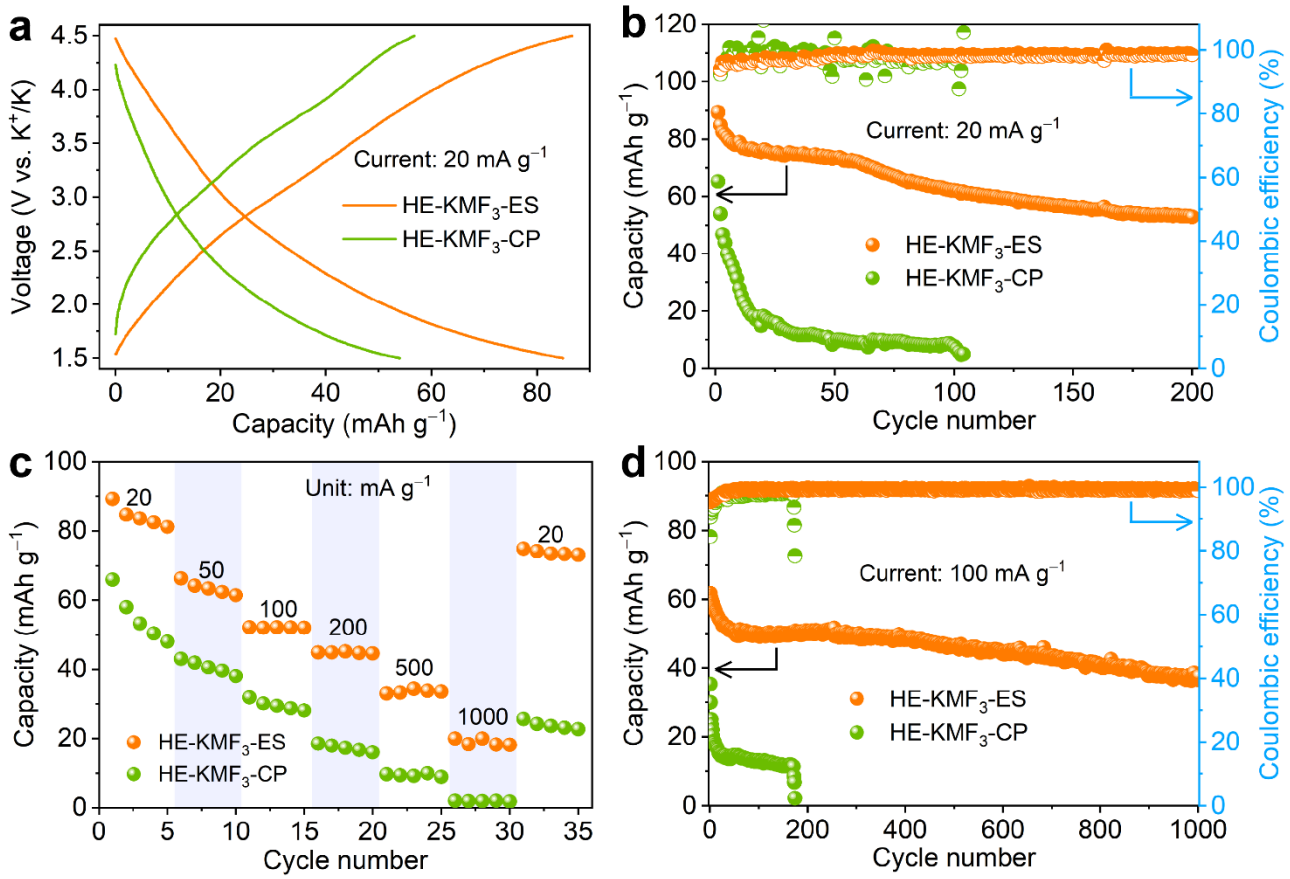

Fig. S27 Comparison of electrochemical performance of HE-KMF_3-ES and HE-KMF_3-CP: (a) typical charge/discharge profiles, (b) cycling performances at 20 mA g^{-1}, (c) rate capabilities, and (d) long-term cycling performance at 100 mA g^{-1}.

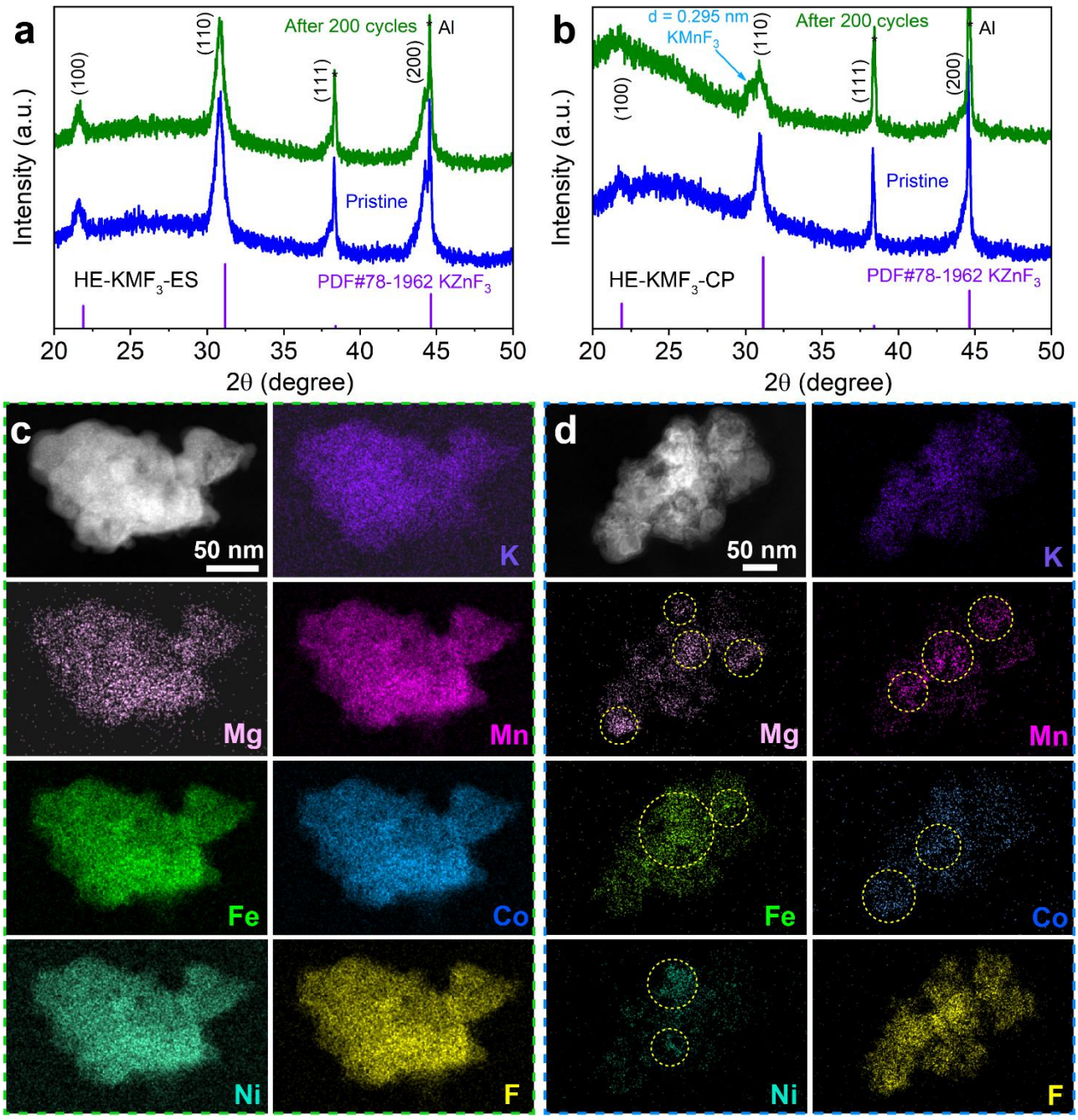

Fig. S28 XRD patterns and elemental mapping of (a, c) HE-KMF_3-ES and (b, d) HE-KMF_3-CP after 200 cycles at 20 mA g^{-1}.

Owing to the uneven distribution of elements in the HE-KMF_3-CP sample, some components decompose, such as $KFeF_3$, which is easily converted into Fe and KF (see Fig. 5f in the main text). After cycling, the XRD peak intensity decreases and the Fe element aggregates. Mn^{2+} is difficult to be reduced, so the peak of $KMnF_3$ obtained through phase transition seems to be more obvious.

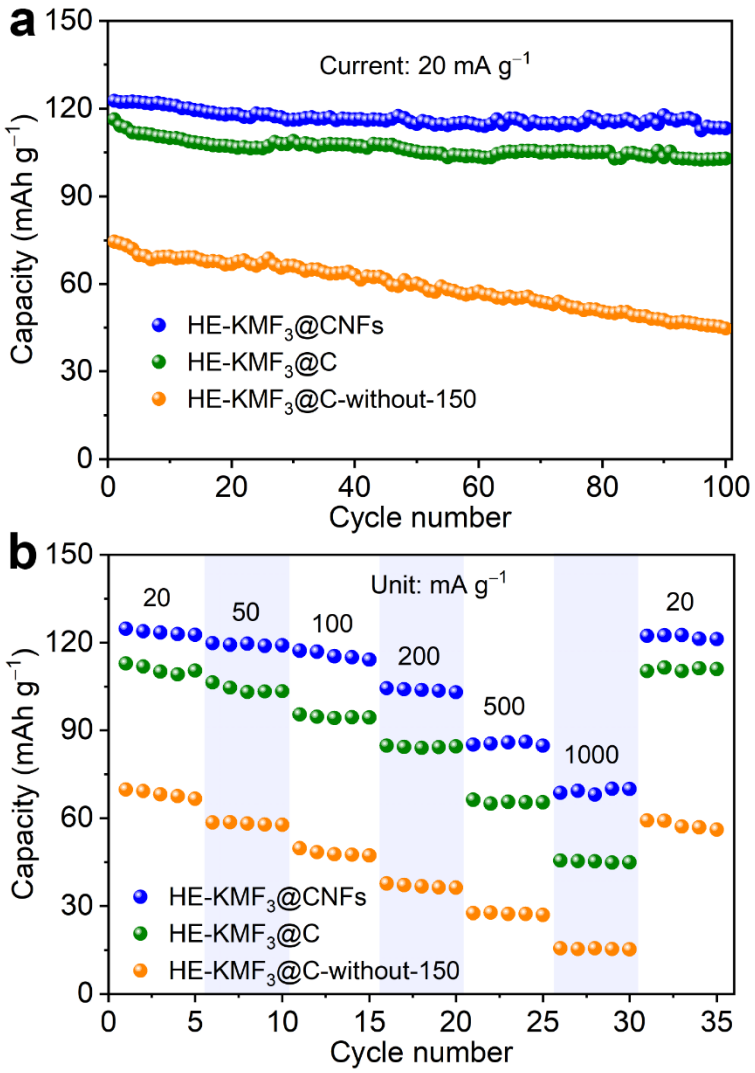

Fig. S29 Electrochemical characterization of HE-KMF_3@C, HE-KMF_3@CNFs, and HE-KMF_3@C-without-150: (a) cycling performances and (b) rate capabilities.

Apparently, HE-KMF_3@C and HE-KMF_3@CNFs (real HE materials) manifested better potassium storage performance than HE-KMF_3@C-without-150 (nominal HE material).

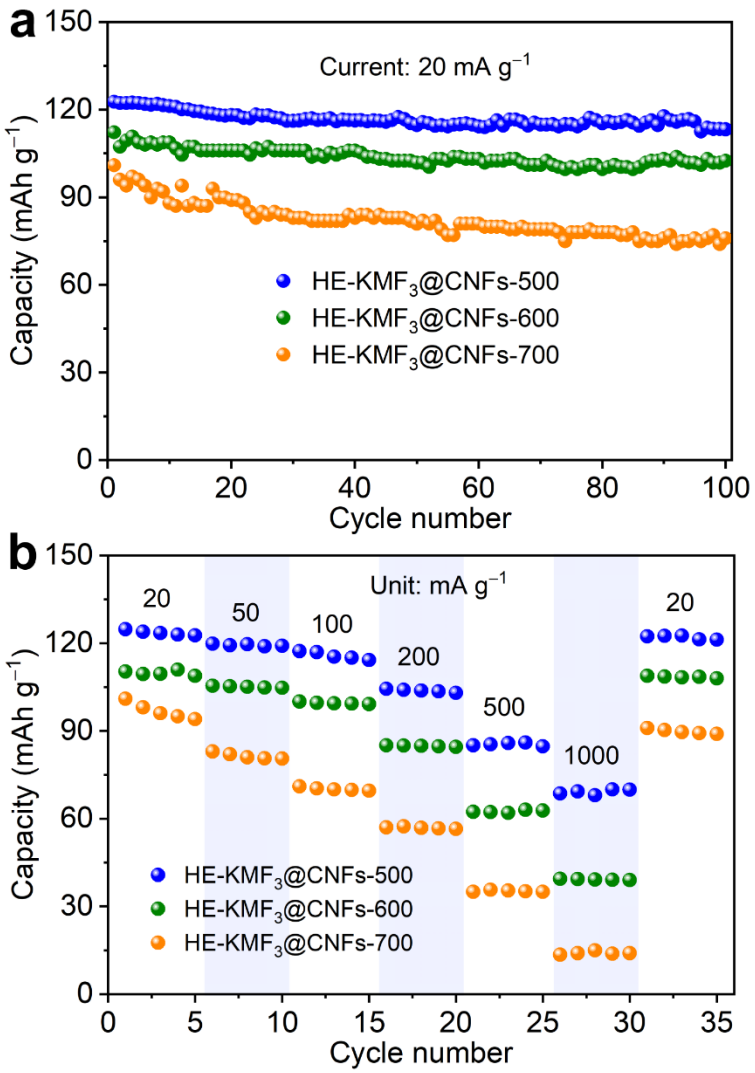

Fig. S30 Electrochemical characterization of HE-KMF_3@CNFs annealed at different temperatures: (a) cycling performances and (b) rate capabilities.

With the increase of annealing temperature from 500 ℃ to 600 and 700 ℃, the average particle size of HE-KMF_3@CNFs increased from 10.4 nm to 28.7 and 48.9 nm, respectively (Fig. S21). The corresponding K storage performances shown in Fig. S30 indicate that the larger the particle size of perovskite fluoride, the worse the reversible capacity and rate performance.

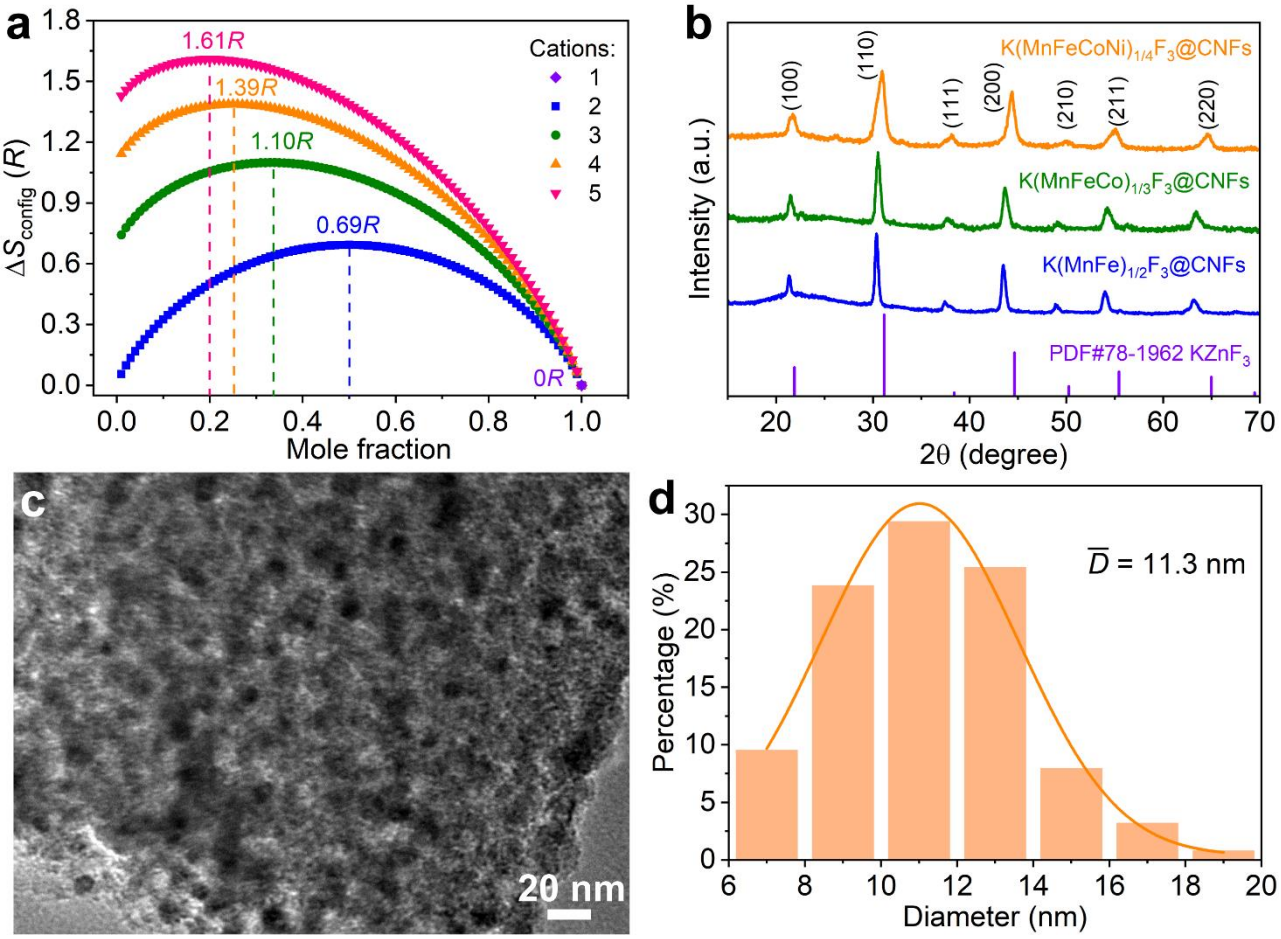

Fig. S31 (a) Dependence of configurational entropy on the number of elements. (b) XRD patterns of multicomponent KMF_3@CNFs with low-entropy (< 1*R*) and medium-entropy (1*R*~1.5*R*). (c) TEM image and (d) size distribution of $K(MnFeCoNi)_{1/4}F_3$@CNFs.

The controlled samples of multicomponent KMF_3@CNFs with low-entropy and medium-entropy were synthesized by adjusting the composition of the M site. The configurational entropy (ΔS_{config}) of KMF_3 was calculated to be 0, 0.69, 1.10, 1.39, and 1.61*R* for $KFeF_3$@CNFs, $K(MnFe)_{1/2}F_3$@CNFs, $K(MnFeCo)_{1/3}F_3$@CNFs, $K(MnFeCoNi)_{1/4}F_3$@CNFs, and $K(MgMnFeCoNi)_{1/5}F_3$@CNFs (i.e., HE-KMF_3@CNFs), respectively. Note that the average particle size of $K(MnFeCoNi)_{1/4}F_3$@CNFs (11.3 nm) is close to HE-KMF_3@CNFs (10.4 nm).

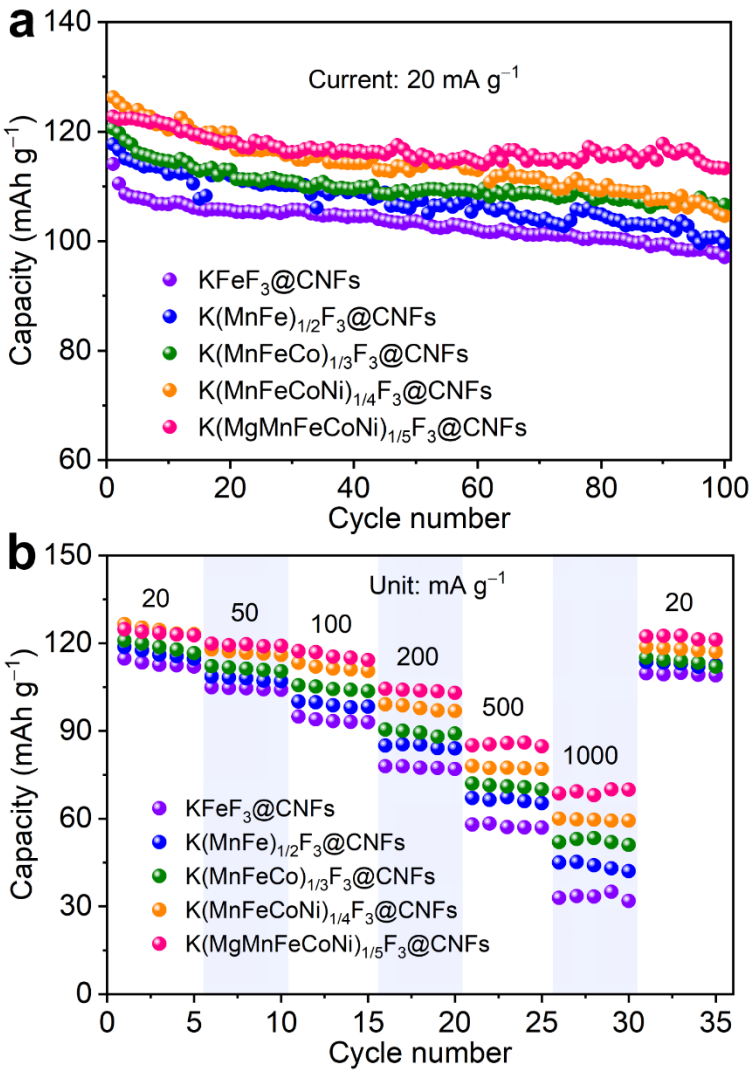

Fig. S32 Electrochemical characterization of multicomponent KMF_3@CNFs: (a) cycling performances and (b) rate capabilities.

Obviously, the high-entropy HE-KMF_3@CNFs exhibits better reversible capacity, cycle stability, and rate performance than the medium-entropy $K(MnFeCo)_{1/3}F_3$@CNFs and $K(MnFeCoNi)_{1/4}F_3$@CNFs and the low-entropy $KFeF_3$@CNFs and $K(MnFe)_{1/2}F_3$@CNFs.

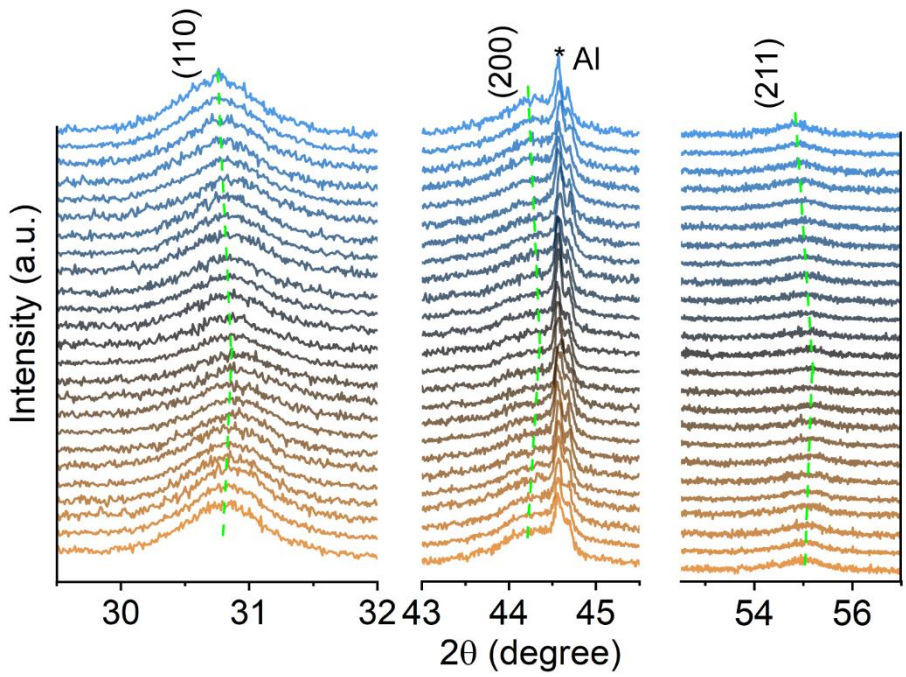

Fig. S33 Enlarged regions of the (110), (200), and (211) peaks of the *in situ* XRD patterns of HE-KMF_3@CNFs during the first cycle.

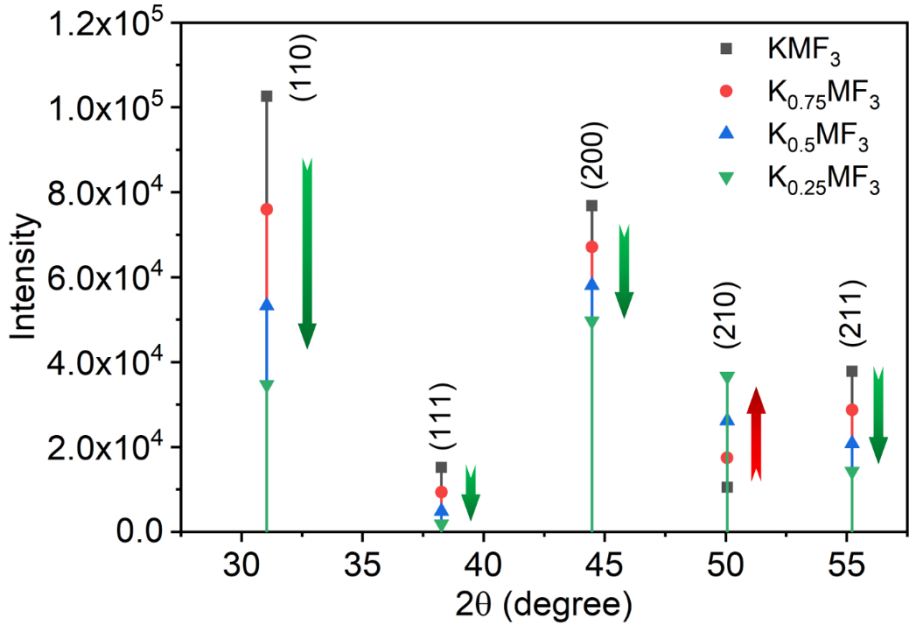

Fig. S34 Simulated XRD patterns of HE-KMF_3@CNFs in different depotassiation states.

As simulated in Fig. S34, the intensities of the (110), (111), (200), and (211) peaks decrease during depotassiation, while the intensity of (210) peak increases.

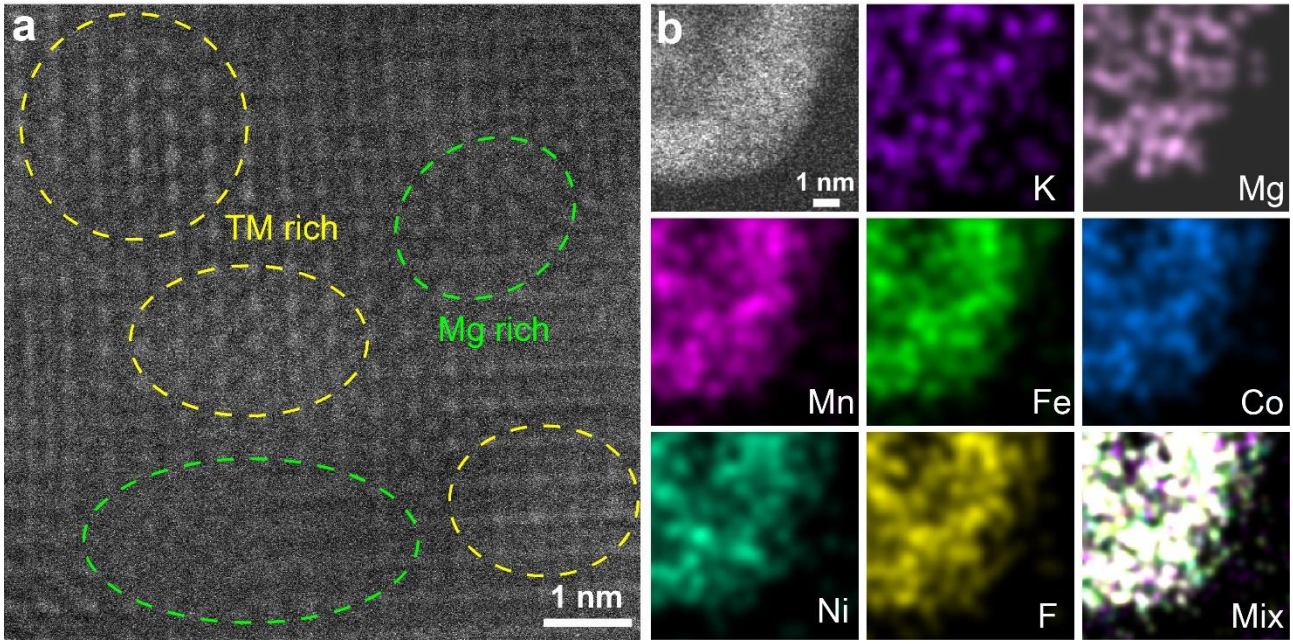

Fig. S35 (a) HAADF-STEM image and (b) elemental mapping of one HE-KMF_3 particle in the fully charged HE-KMF_3@CNFs.

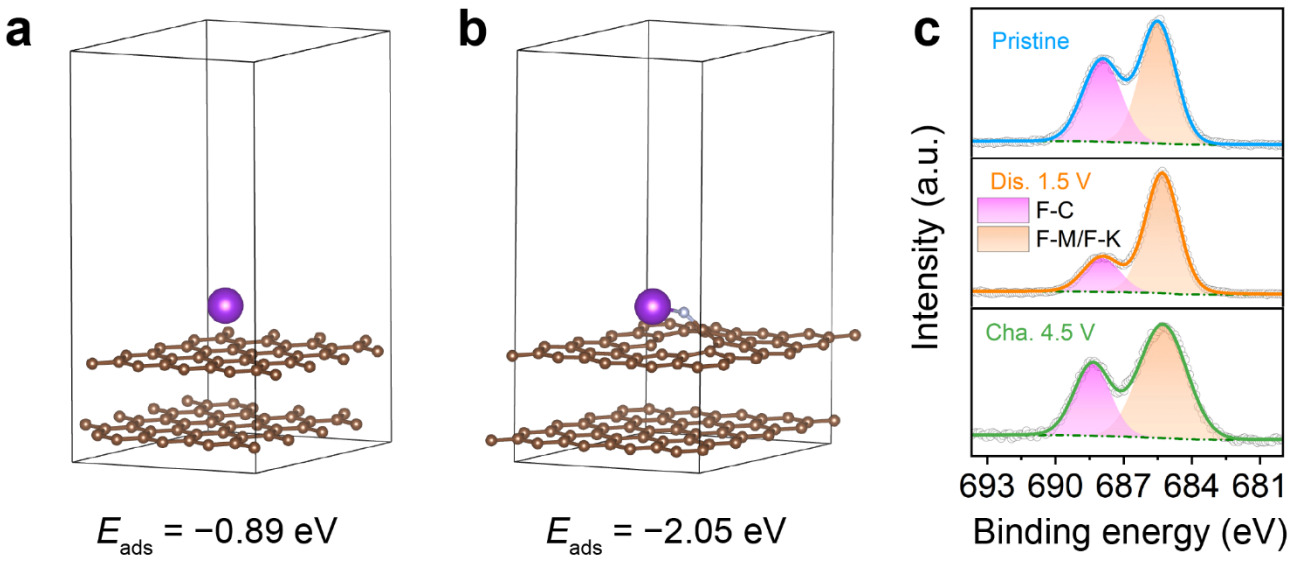

Fig. S36 DFT calculations of potassium ion adsorption energies on (a) pristine carbon and (b) F-dopped carbon. (c) XPS spectra of F 1s of HE-KMF_3@CNFs in different states (Note that freestanding electrodes are used to avoid the interference from the binder PVDF).

DFT calculations indicate that the potassium ion adsorption energy of pristine carbon is approximately −0.89 eV, while it drops to −2.05 eV in F-dopped carbon (Fig. S36). The potassium storage voltage of pristine carbon is generally between 0.01 to 1.5 V. However, the F-dopped carbon with stronger potassium ions adsorption ability can increase the voltage above 1.5 V.

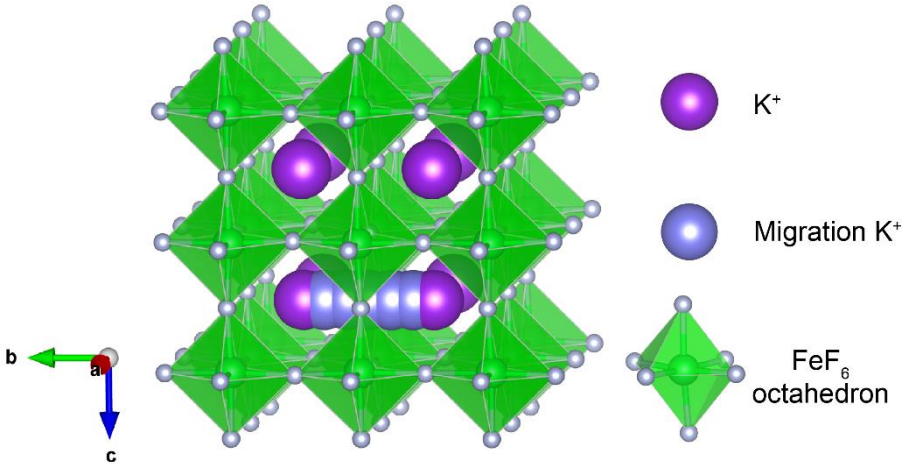

Fig. S37 Calculated K^+ diffusion path along the *b* orientation in $KFeF_3$.

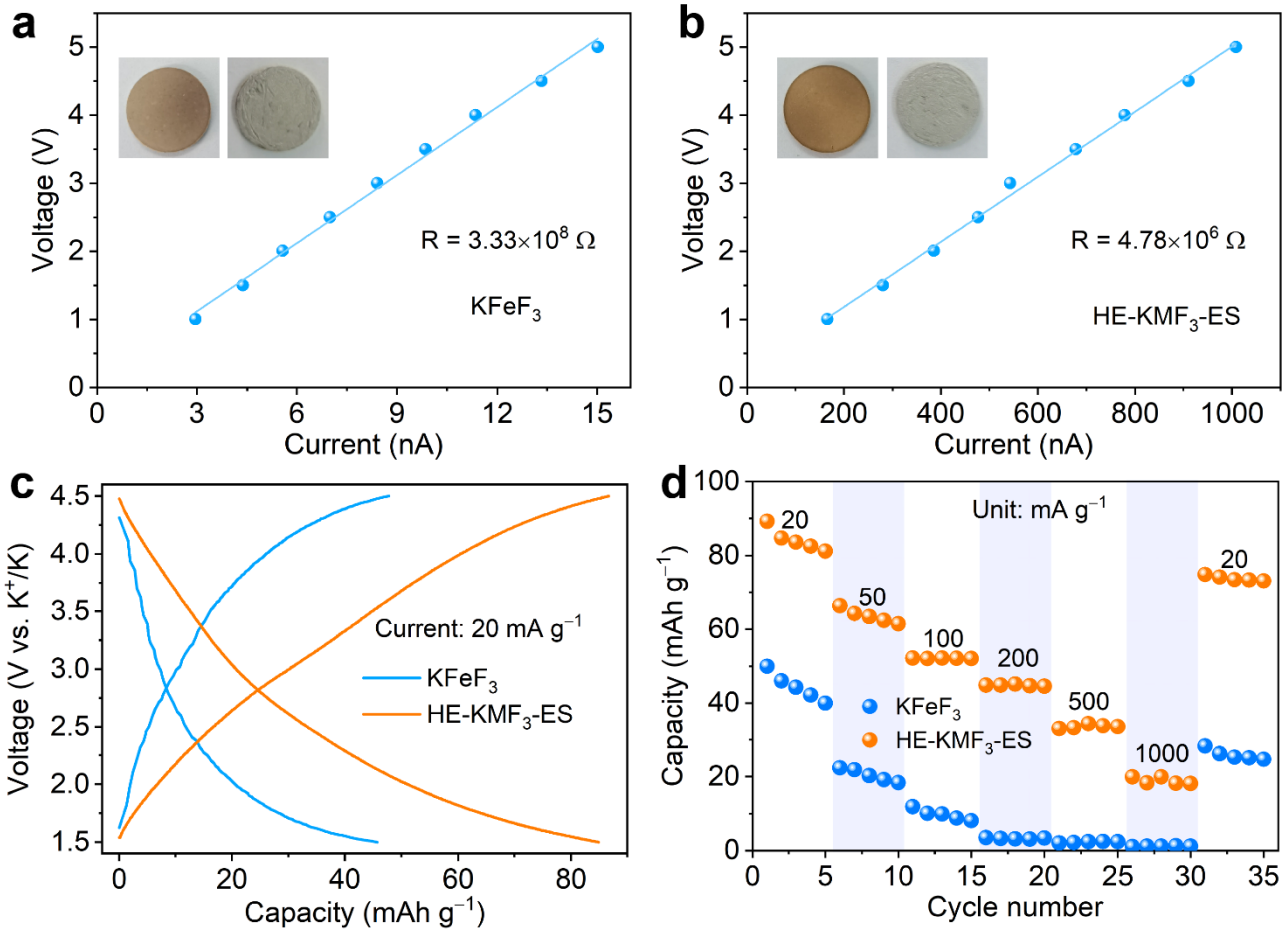

Fig. S38 Liner fitting of *U–I* curves: (a) $KFeF_3$ and (b) HE-KMF_3-ES. Insets in (a and b) are photographs of the pellets before (left) and after (right) pasting with silver conductive paste, respectively. Comparison of electrochemical performance of $KFeF_3$ and HE-KMF_3-ES: (c) typical charge/discharge profiles and (d) rate capability.

The electronic conductivity of $KFeF_3$ (1.95×10^{-10} S cm^{-1}) and HE-KMF_3-ES (1.38×10^{-8} S cm^{-1}) can be calculated based on the following equation:

$$\sigma = \frac{L}{SR} \tag{4}$$

where L is the thickness of the pellet (0.1 cm), S is the area of the pellet (1.539 cm^2), and R is the resistance of the pellet.

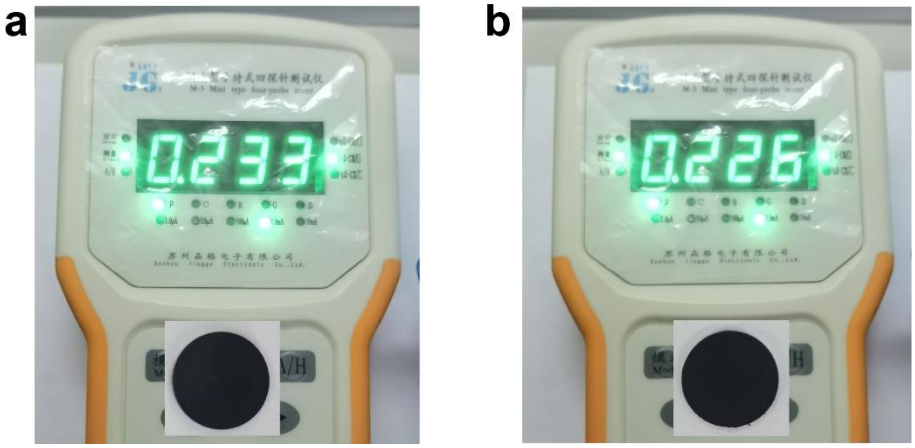

Fig. S39 Digital images of the resistivity of (a) $KFeF_3$@CNFs (0.233 Ω cm) and (b) HE-KMF_3@CNFs (0.226 Ω cm) measured using the M-3 Mini type four-probe tester. Insets in (a and b) are photographs of the samples.

Owing to the low resistance of CNFs, the four-probe tester was used to measure the electronic conductivity of $KFeF_3$@CNFs and HE-KMF_3@CNFs to reduce the impact of contact resistance. The calculated electronic conductivity of $KFeF_3$@CNFs (4.29 S cm^{-1}) is close to HE-KMF_3@CNFs (4.42 S cm^{-1}), but much higher than that of $KFeF_3$ (1.95×10^{-10} S cm^{-1}) and HE-KMF_3-ES (1.38×10^{-8} S cm^{-1}).

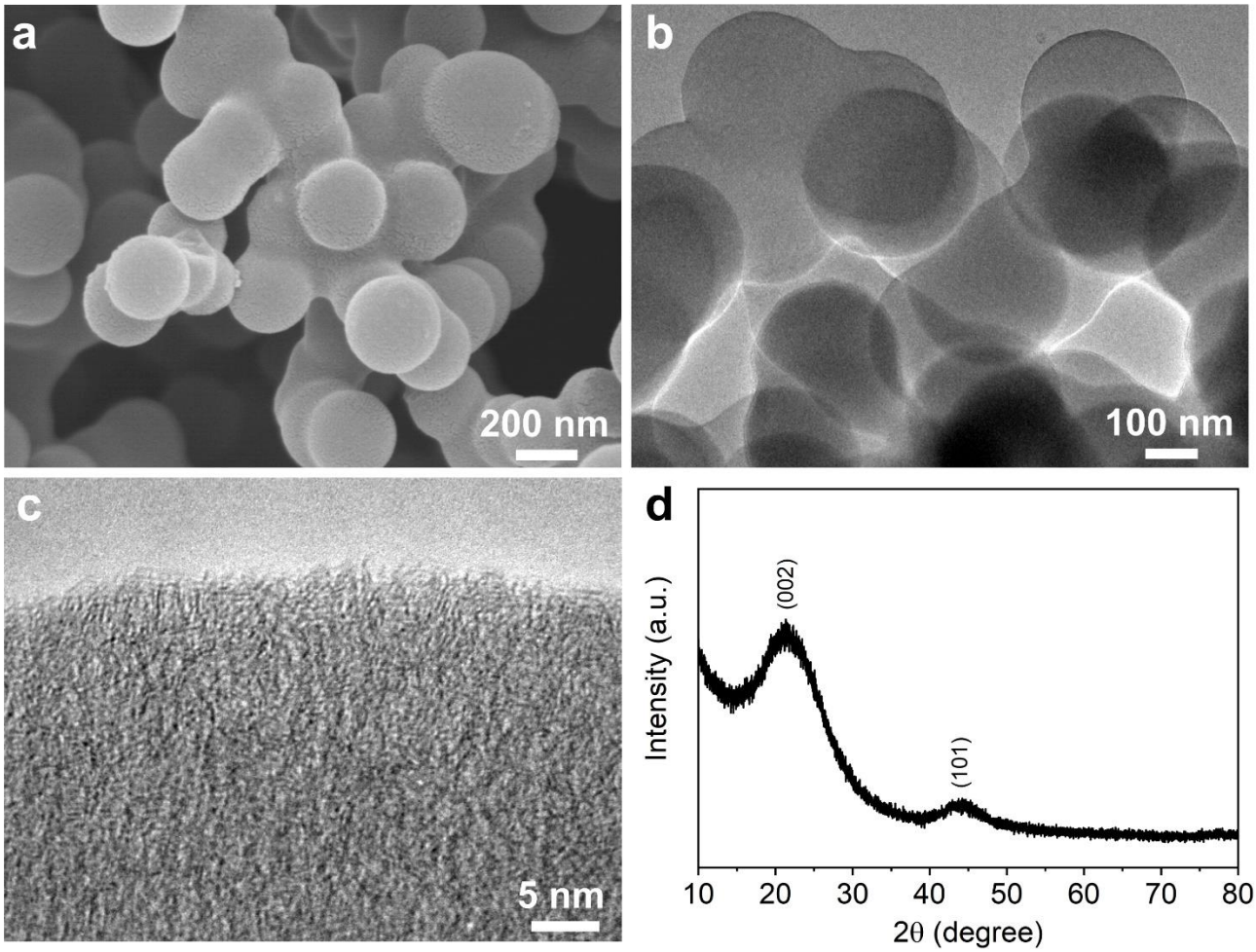

Fig. S40 (a) SEM image, (b) TEM image, (c) HRTEM image, and (d) XRD pattern of HCS.

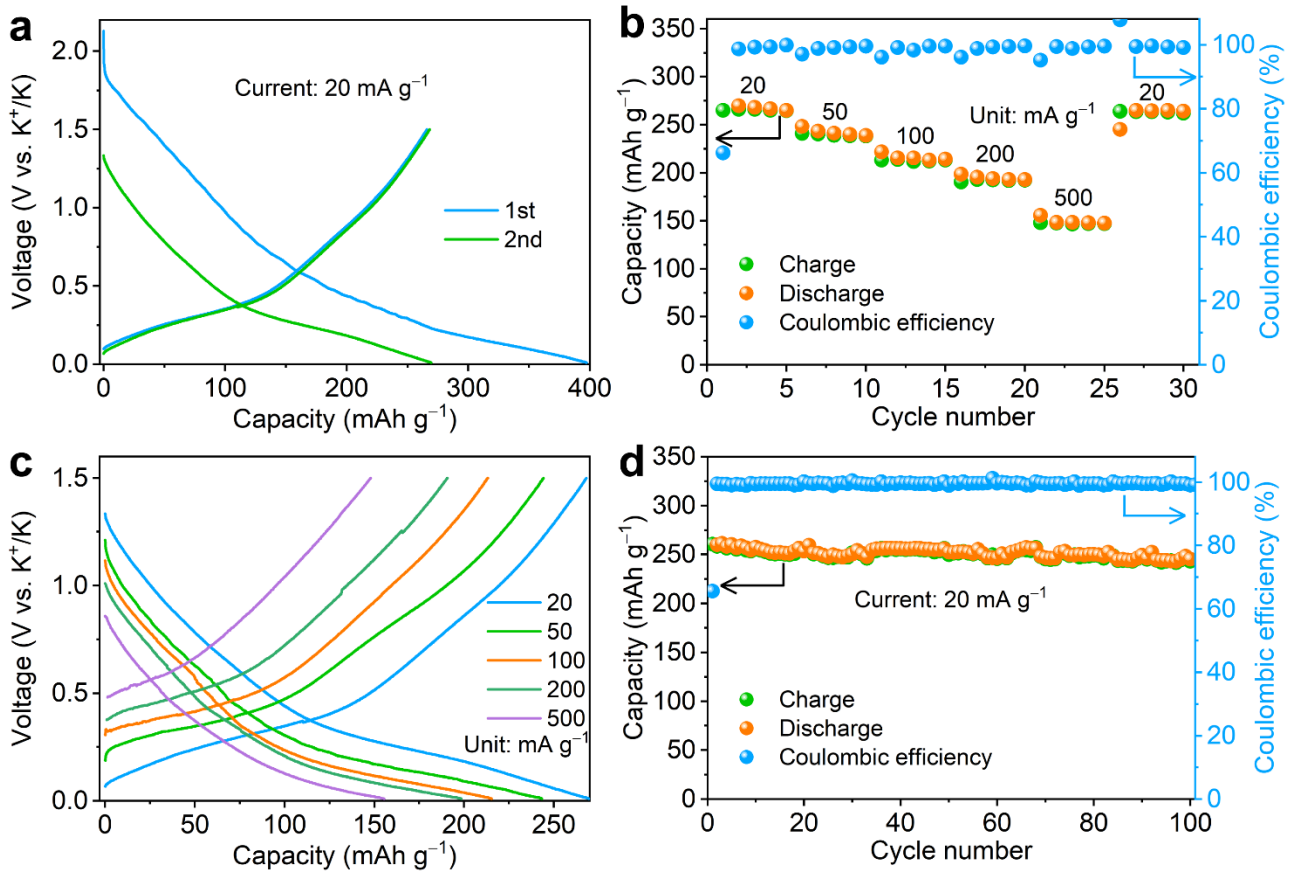

Fig. S41 Potassium storage properties of HCS: (a) charge/discharge curves at 20 mA g^{-1}, (b) rate capability, (c) charge–discharge profiles at different current densities, and (d) cycling performance at 20 mA g^{-1}.

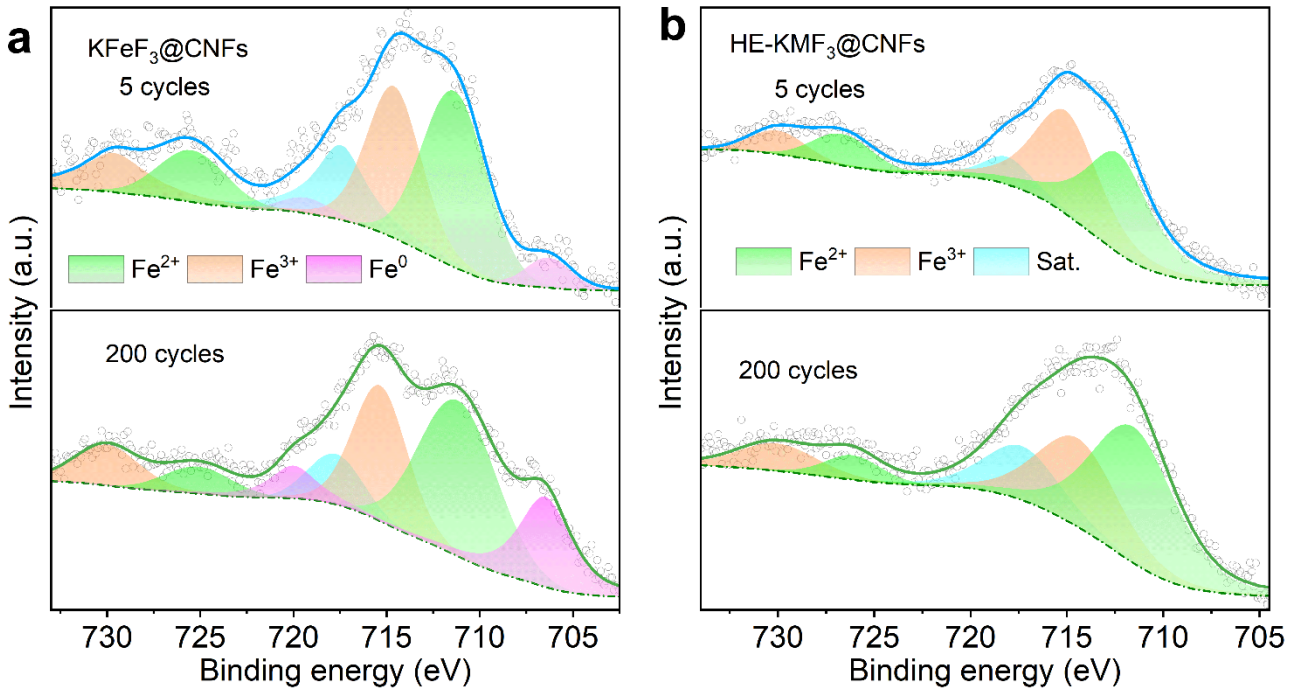

Fig. S42 Comparison of XPS spectra of the (a) $KFeF_3$@CNFs and (b) HE-KMF_3@CNFs electrodes after 5 and 200 cycles.

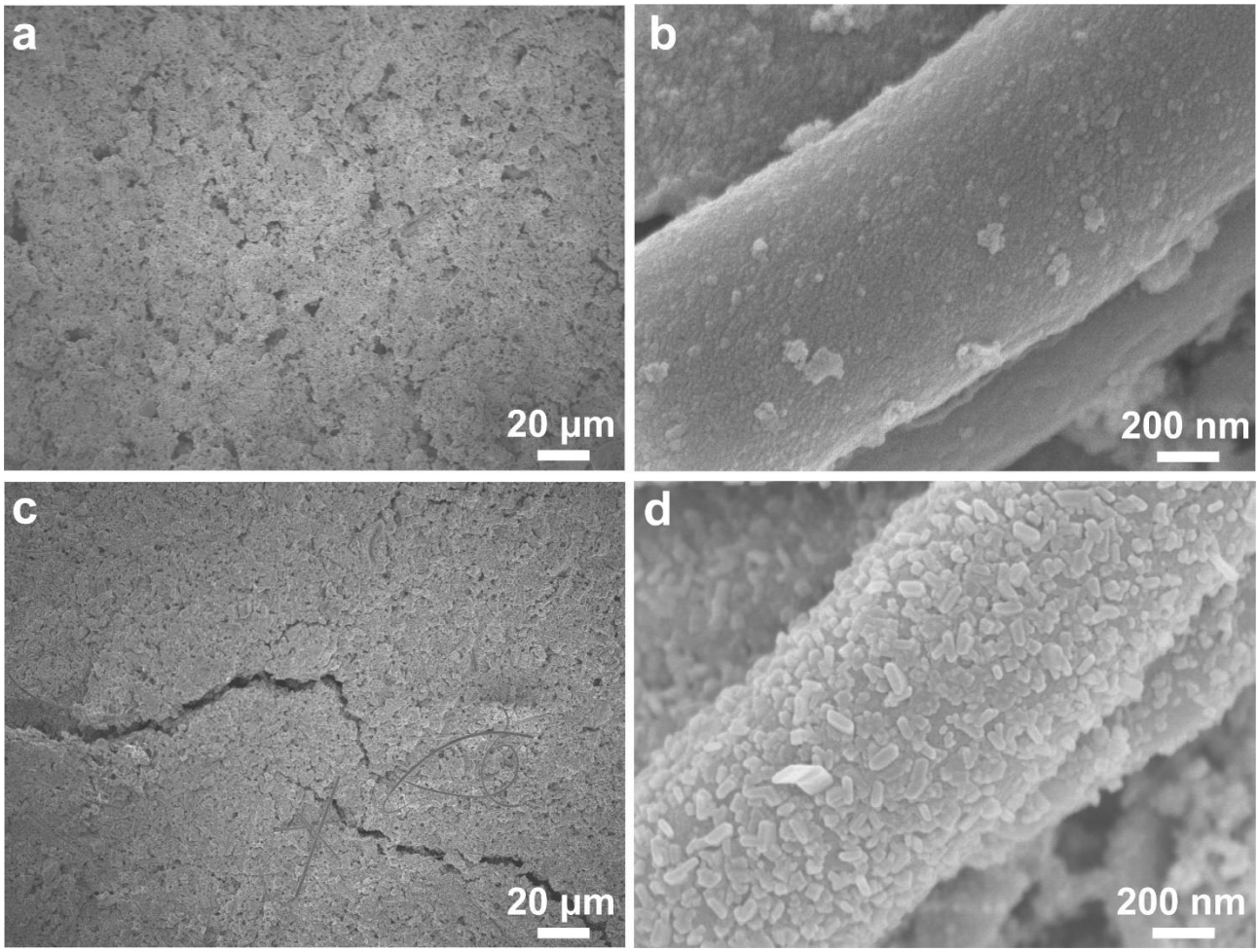

Fig. S43 SEM images of (a, b) the pristine $KFeF_3$@CNFs electrode and (c, d) the $KFeF_3$@CNFs electrode after 200 cycles.

After 200 cycles, the $KFeF_3$@CNFs electrode showed obvious degradation and large cracks (Fig. S43c), and the surface of CNFs was occupied by by-products (Fig. S43d). In contrast, the HE-KMF_3@CNFs electrode was almost intact (see below, Fig. S44).

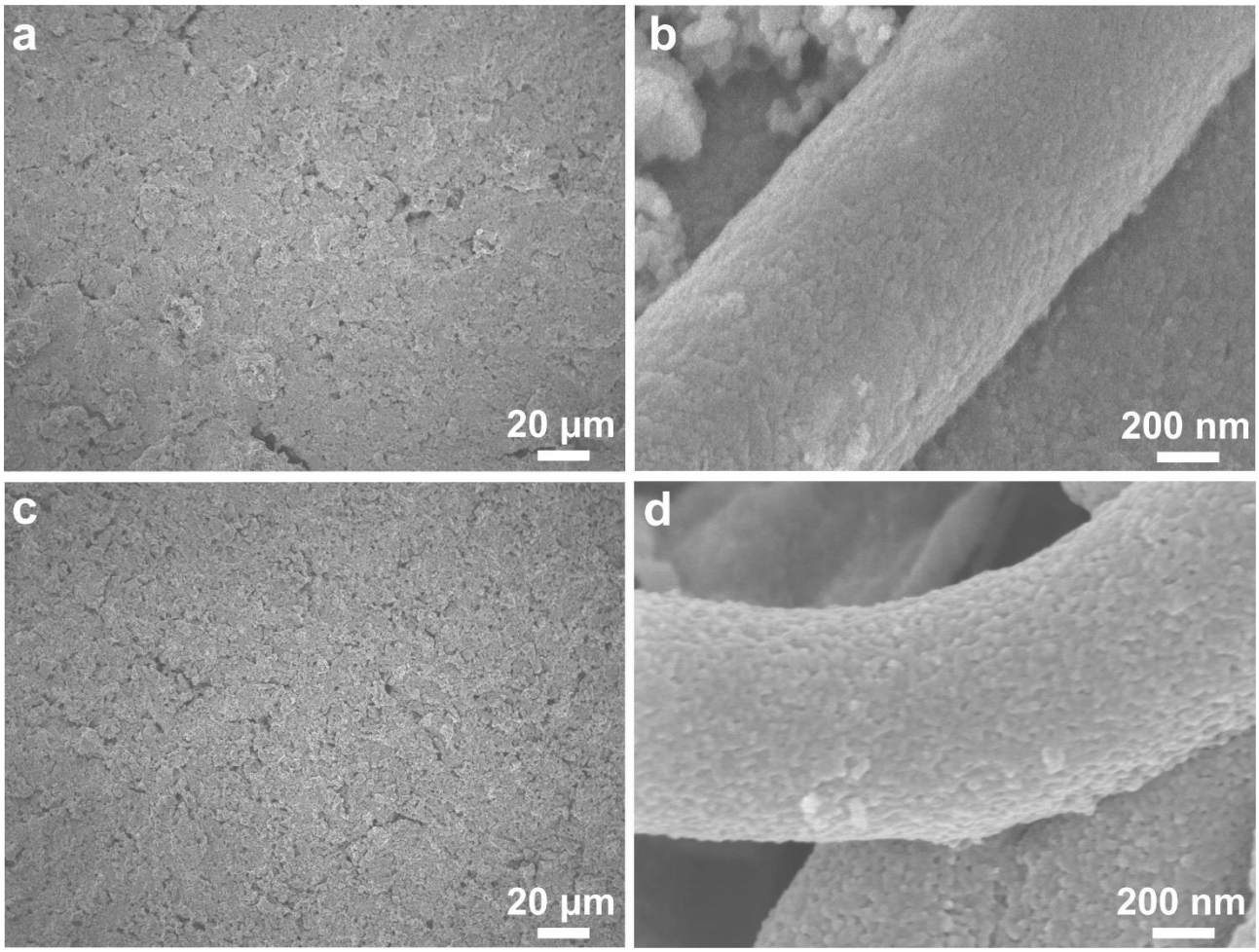

Fig. S44 SEM images of (a, b) the pristine HE-KMF_3@CNFs electrode and (c, d) the HE-KMF_3@CNFs electrode after 200 cycles.

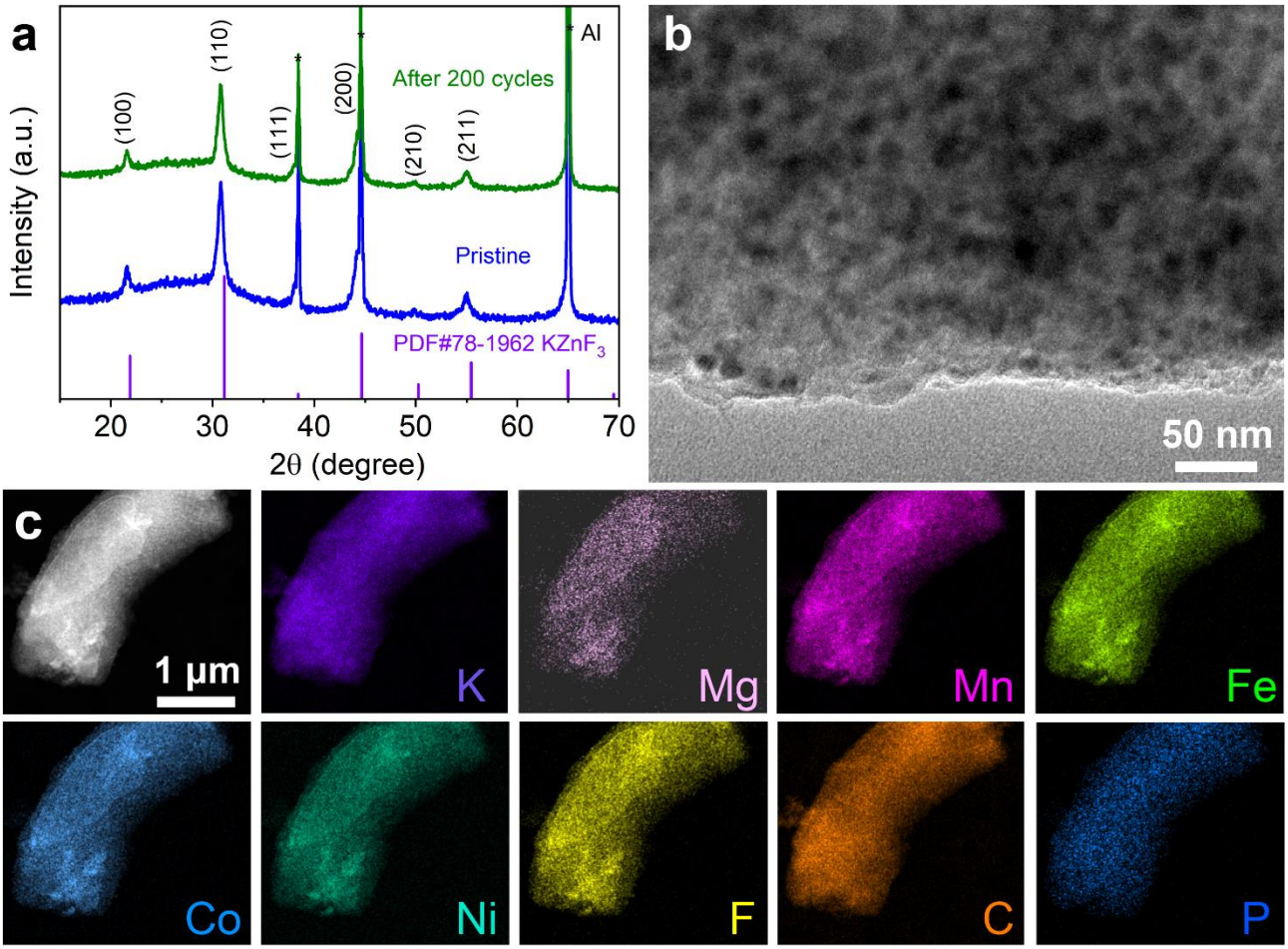

Fig. S45 Characterization of the HE-KMF_3@CNFs electrode after 200 cycles: (a) XRD pattern comparison with the pristine electrode, (b) TEM image, and (c) elemental mapping.

The XRD pattern of the HE-KMF_3@CNFs electrode after 200 cycles was collected, demonstrating the well-preserved crystal architecture (Fig. S45a). The nanoparticles of HE-KMF_3 and K, Mg, Mn, Fe, Co, Ni, and F elements were uniformly distributed in CNFs (Fig. S45b and c), indicating that the HE structure was well maintained.

Table S1. Crystallographic data and parameters of the Rietveld refinement for HE-KMF_3@CNFs.

Formula	$KMg_{0.2}Mn_{0.2}Fe_{0.2}Co_{0.2}Ni_{0.2}F_3$
Space group	$Pm\bar{3}m$
a, Å	4.0818(5)
V, $Å^3$	68.009(7)
Z	1
χ^2	1.72
R_{wp}, R_p	3.5%, 2.8%
Radiation	X-ray, Cu Kα
	λ_1 = 1.54051 Å, λ_2 = 1.54433 Å
2θ range, step, deg.	15–90, 0.01

Table S2. Fractional atomic coordinates and atomic displacement parameters of HE-KMF_3@CNFs.

Atom	Position	Occupancy	x	y	z	U_{iso}
K	1a	1	0	0	0	0.021
Mg	1b	0.2	0.5	0.5	0.5	0.032
Mn	1b	0.2	0.5	0.5	0.5	0.032
Fe	1b	0.2	0.5	0.5	0.5	0.032
Co	1b	0.2	0.5	0.5	0.5	0.032
Ni	1b	0.2	0.5	0.5	0.5	0.032
F	3c	1	0	0.5	0.5	0.025

Table S3. Lattice parameters of KMF_3@CNFs (M = Mn, Fe, Co, Ni, Mg, and HE).

Sample	Ionic radius of M^{2+}/Å	*a*/Å
$KMnF_3$@CNFs	0.83	4.17
$KFeF_3$@CNFs	0.78	4.11
$KCoF_3$@CNFs	0.745	4.07
$KNiF_3$@CNFs	0.69	4.03
$KMgF_3$@CNFs	0.72	3.99
HE-KMF_3@CNFs	0.753 (average)	4.08

Table S4. Calculated formation energies of different interface models between graphene and the (100), (110), (111), or (211) plane of HE-KMF_3.

Surface	Model	E_{total}/eV	$E_{surface}$/eV	$E_{graphene}$/eV	ΔE/eV	$E_{formation}$/eV*
(100)	1	−411.295	−191.438	−219.012	−0.845	−0.845
(100)	2	−410.987	−191.438	−219.012	−0.537	−0.537
(100)	3	−411.445	−191.783	−219.012	−0.650	−0.650
(110)	1	−745.34	−382.033	−365.02	1.713	1.117
(110)	2	−748.94	−382.033	−365.02	−1.887	−1.231
(110)	3	−747.69	−381.239	−365.02	−1.431	−0.933
(111)	1	−837.064	−380.393	−456.275	−0.396	−0.241
(111)	2	−831.966	−373.73	−456.275	−1.961	−1.193
(111)	3	−831.423	−373.73	−456.275	−1.418	−0.863
(211)	1	−1037.204	−380.756	−657.036	0.588	0.217
(211)	2	−1036.753	−380.756	−657.036	1.039	0.384

*Note that $E_{formation}$ is calculated by normalizing to the unit area of the (100) surface.

Table S5. Calculated formation energies of graphene acting on the (110) or (111) surface of KMF_3 (M = Mg, Mn, Fe, Co, and Ni).

Sample	Surface	E_{total}/eV	$E_{surface}$/eV	$E_{graphene}$/eV	ΔE/eV	$E_{formation}$/eV*
Mg	(110)	−551.195	−184.584	−365.020	−1.591	−1.078
	(111)	−639.293	−181.144	−456.275	−1.874	−1.025
Mn	(110)	−564.241	−198.296	−365.020	−0.925	−0.650
	(111)	−653.160	−196.782	−456.275	−0.103	−0.056
Fe	(110)	−555.060	−188.860	−365.020	−1.180	−0.799
	(111)	−645.134	−188.146	−456.275	−0.713	−0.390
Co	(110)	−547.556	−181.871	−365.020	−0.665	−0.450
	(111)	−637.118	−180.068	−456.275	−0.775	−0.424
Ni	(110)	−536.615	−170.704	−365.020	−0.891	−0.603
	(111)	−626.352	−169.124	−456.275	−0.953	−0.521

*Note that $E_{formation}$ is computed by normalizing to the unit area of the (100) plane.

Table S6. Comparison of conventional electrode and self-supporting electrodes with different mass loadings of HE-KMF_3@CNFs.

	Mass loading (mg cm^{-2})	Specific capacity (mAh g^{-1})	Areal capacity (mAh cm^{-2})	Areal energy density (mWh cm^{-2})
Conventional electrode	2.0	122.0	0.24	0.59
	5.0	120.7	0.60	1.47
Self-supporting electrode	7.7	118.2	0.91	2.18
	10.8	117.3	1.27	3.05

Table S7. Synthesis and electrochemical performance of various perovskite fluorides reported in potassium-ion batteries.

Composition	Synthetic method	Post-processing	Cycles/capacity/current density (mAh g^{-1}/mA g^{-1})	Rate capability (mAh g^{-1}/mA g^{-1})	Reference
$KFeF_3$/KB	Coprecipitation	Ball milling	100/61/90	61/90	[6]
$KFeF_3$/rGO	Solvothermal	Carbon coating	1000/60/500	53/500	[7]
$KFeF_3$/AB	Sol-gel	Ball milling	50/124/20	Not reported	[8]
NH_4FeF_3/AB	Sol-gel	Ball milling	30/113/20	Not reported	[8]
$KMnO_{0.125}F_{2.875}$/C	Coprecipitation	Carbon coating	200/80/100	80/100	[9]
$KMn_{0.95}Co_{0.05}F_3$	Coprecipitation	None	200/100/35	Not reported	[10]
$KMn_{10/11}Co_{1/11}F_3$	Coprecipitation	Ball milling	60/110/40	Not reported	[11]
HE-KMF_3@CNFs	Electrospinning & pyrolysis	None	200/122/20 1000/113/100 5000/85/500	70/1000	This work

KB: Ketjen black; rGO: reduced graphene oxide; AB: acetylene black.

Table S8. Calculated Gibbs free energy.

Component	$KFeF_3$	HE-KMF_3	K^+	KF	Mg	Mn	Fe	Co	Ni
Gibbs free energy (eV)	–24.381	–24.374	–4.030	–8.296	–1.512	–8.910	–7.724	–6.830	–5.426

$KFeF_3 + 2K^+ + 2e^- \leftrightarrow 3KF + Fe \qquad \Delta G = -0.17$ eV

$KMg_{0.2}Mn_{0.2}Fe_{0.2}Co_{0.2}Ni_{0.2}F_3 + 2K^+ + 2e^- \leftrightarrow 3KF + 0.2Mg + 0.2Mn + 0.2Fe + 0.2Co + 0.2Ni$

$\Delta G = 1.48$ eV

Table S9. Electrochemical performance comparison of the HE-KMF_3@CNFs//HCS full cell and previously reported potassium-ion full cells.

Full cell	Working voltage (V)	Capacity (mAh g^{-1})*	Cycling stability (retention/cycles/mA g^{-1})	Rate capability (retention/mA g^{-1})	Reference
PTCDA//TQBQ-COF	~1.5	85	77.4%/50/600	64.5%/600	[12]
PTCDA//Bi-MOF	~1.8	76	74%/100/500	50.1%/1500	[13]
PTCDA//BiSb-HTR	~1.8	97	39.7%/100/1000	23.4%/10000	[14]
PTCDA//BCO/rGO	~2.0	103	80.4%/200/300	30%/200	[15]
PTCDA//KC_8	~1.6	87	84.1%/100/30	65.4%/2000	[16]
$K_{0.5}MnO_2$//SC	~2.2	73	88.7%/100/10	27.7%/500	[17]
$K_{0.45}Mn_{0.9}Al_{0.1}O_2$//SC	~1.9	82	95%/120/100	42.9%/500	[18]
VO_2//Gr	~1.5	81	82%/200/200	56.3%/500	[19]
$K_{0.6}CoO_2$//SC	2.3	61	79%/300/20	57%/200	[20]
$K_{0.35}Mn_{0.8}Fe_{0.1}Cu_{0.1}O_2$ //Gr	~1.7	61	97%/300/100	85.6%/500	[21]
$KFeC_2O_4F$//SC	~2.85	59	~100%/200/100	74.8%/500	[22]
$KVPO_4F$//SC	3.66	64	80.3%/500/50	72.5%/2000	[23]
KVNP//KVNP	3.13	40	72%/90/10	Not reported	[24]
$KFeSO_4F$//Gr	3.41	71	89.5%/600/128	57.2%/2560	[25]
KVP//PANI-LT	3.06	49	81.9%/600/100	65.3%/1000	[26]
KMnHCF-EDTA//Gr	3.58	93	98.5%/300/30	50.8%/1250	[27]
KNiHCF//Gr	2.84	34	87.1%/500/500	82.8%/5000	[28]
KMnHCF//Gr	3.5	74	80%/1000/62.5	70%/625	[29]
KFeHCF//O-Sb-N SA@NC	~2.6	48	81%/1200/5000	40%/5000	[30]
KMnHCF-S//Gr	3.62	86	90.2%/1500/100	72.1%/400	[31]
HE-KMF_3@CNFs//HCS	1.60	77	74.5%/2000/500	61.0%/500	This work

PTCDA: perylene-3,4,9,10-tetracarboxylic dianhydride; TQBQ-COF: triquinoxalinylene and benzoquinone covalent organic framework; Bi-MOF: Bi and terephthalic metal–organic framework; BiSb-HTR: high-temperature thermal radiation synthesized BiSb; BCO: $(BiO)_2CO_3$; SC: soft carbon; Gr: graphite; KVNP: $K_{0.76}V_{0.55}Nb_{0.45}OPO_4$; KVP: $K_3(VO)(HV_2O_3)(PO_4)_2(HPO_4)$; PANI-LT: polyaniline-intercalated layered titanate; KNiHCF: $K_{1.84}Ni[Fe(CN)_6]_{0.88}\cdot 0.49H_2O$; KMnHCF-EDTA: $K_{1.94}Mn[Fe(CN)_6]_{0.994}\cdot 0.08H_2O$; KFeHCF: $K_{1.92}Fe[Fe(CN)_6]_{0.88}\cdot 0.5H_2O$; O-Sb-N SA@NC: single-atom Sb dispersed in nitrogen-doped porous carbon nanosheets.

*Note that capacity is calculated based on the total mass of cathode and anode materials: $C_{total} = 1/(1/C_{cathode} + 1/C_{anode})$.

References

1. T. Wang, H. Chen, Z. Yang, J. Liang and S. Dai, *J. Am. Chem. Soc.*, 2020, **142**, 4550–4554.
2. Z. Jian, Z. Xing, C. Bommier, Z. Li and X. Ji, *Adv. Energy Mater.*, 2016, **6**, 1501874.
3. S. Chu, C. Shao, J. Tian, J. Wang, Y. Rao, C. Xu, H. Zhou and S. Guo, *ACS Nano*, 2024, **18**, 337–346.
4. Z. W. Chen, J. Li, P. Ou, J. E. Huang, Z. Wen, L. Chen, X. Yao, G. Cai, C. C. Yang, C. V. Singh and Q. Jiang, *Nat. Commun.*, 2024, **15**, 359.
5. L. Duan, C. Shao, J. Liao, L. Song, Y. Zhang, R. Li, S. Guo, X. Zhou and H. Zhou, *Angew. Chem. Int. Ed.*, 2024, **63**, e202400868.
6. D. Cao, C. Yin, D. Shi, Z. Fu, J. Zhang and C. Li, *Adv. Funct. Mater.*, 2017, **27**, 1701130.
7. S. Wang, F. Chen, L.-M. Zhang, Y.-X. Li, N.-Q. Ren, K. Cao, J.-C. Xiao and C.-H. Chen, *Nanoscale*, 2022, **14**, 5347–5355.
8. A. Martin, E. S. Santiago, E. Kemnitz and N. Pinna, *ACS Appl. Mater. Interfaces*, 2019, **11**, 33132–33139.
9. S. Wang, Y. Chen, B. Cui, B. Li, S. Wang, Y. Cui, Z. Ju and Q. Zhuang, *Appl. Surf. Sci.*, 2020, **514**, 145954.
10. S. Wang, X. Zou, C. Li, H. Zheng, B. Li and Q. Zhuang, *J. Power Sources*, 2021, **495**, 229721.
11. S. Wang, B. Cui, Q. Zhuang, Y. Shi and H. Zheng, *J. Electrochem. Soc.*, 2019, **166**, A1819–A1826.

12. X.-L. Chen, M. Xie, Z.-L. Zheng, X. Luo, H. Jin, Y.-F. Chen, G.-Z. Yang, D.-S. Bin and D. Li, *J. Am. Chem. Soc.*, 2023, **145**, 5105–5113.
13. S. Li, Q. Zheng, H. Deng, S. Chen, X. Shen, Y. Yuan, Y. Cheng, J. Zhu and B. Lu, *Small Methods*, 2023, **7**, 2201554.
14. S. Dou, J. Xu, D. Zhang, W. Liu, C. Zeng, J. Zhang, Z. Liu, H. Wang, Y. Liu, Y. Wang, Y. He, W.-D. Liu, W. Gan, Y. Chen and Q. Yuan, *Angew. Chem. Int. Ed.*, 2023, **62**, e202303600.
15. L. Wang, B. Zhang, B. Wang, S. Zeng, M. Zhao, X. Sun, Y. Zhai and L. Xu, *Angew. Chem. Int. Ed.*, 2021, **60**, 15381–15389.
16. L. Liang, M. Tao, Q. Zhu, W. Wei, S. Wang, J. Wang, J. Chen, D. Yu and H. Wang, *Adv. Energy Mater.*, 2023, **13**, 2300453.
17. S. Zhao, Z. Liu, G. Xie, Z. Guo, S. Wang, J. Zhou, X. Xie, B. Sun, S. Guo and G. Wang, *Energy Environ. Sci.*, 2022, **15**, 3015–3023.
18. Y. Huang, X. Zhang, H. Lin, Z. Wei, Y. Zeng, X. Ge, W. Zhang, X. Wang, X. Jin, Z. X. Shen and F. Du, *Chem. Eng. J.*, 2023, **453**, 139571.
19. L. Wu, H. Fu, S. Li, J. Zhu, J. Zhou, A. M. Rao, L. Cha, K. Guo, S. Wen and B. Lu, *Nat. Commun.*, 2023, **14**, 644.
20. Z. Zhang, Q. Hu, J. Liao, Y. Xu, L. Duan, R. Tian, Y. Du, J. Shen, and X. Zhou, *Nano Lett.*, 2023, **23**, 694–700.
21. J. Lv, B. Wang, J. Hao, H. Ding, L. Fan, R. Tao, H. Yang, J. Zhou and B. Lu, *eScience*, 2023, **3**, 100081.
22. B. Ji, W. Yao, Y. Zheng, P. Kidkhunthod, X. Zhou, S. Tunmee, S. Sattayaporn, H.-M. Cheng, H. He and Y. Tang, *Nat. Commun.*, 2020, **11**, 1225.
23. J. Liao, X. Zhang, Q. Zhang, Q. Hu, F. Li, Y. Du, J. Xu, L. Gu and X. Zhou, *Nano Lett.*, 2022, **22**, 4933–4940.
24. J. Bao, W. Deng, J. Liu and C.-F. Sun, *Energy Storage Mater.*, 2021, **42**, 806–814.
25. J. Liao, Q. Hu, Y. Du, J. Li, L. Duan, J. Bao and X. Zhou, *Sci. Bull.*, 2022, **67**, 2208–2215.
26. J. Liao, C. Chen, Q. Hu, Y. Du, Y. He, Y. Xu, Z. Zhang and X. Zhou, *Angew. Chem. Int. Ed.*, 2021, **60**, 25575–25582.

27. L. Deng, J. Qu, X. Niu, J. Liu, J. Zhang, Y. Hong, M. Feng, J. Wang, M. Hu, L. Zeng, Q. Zhang, L. Guo and Y. Zhu, *Nat. Commun.*, 2021, **12**, 2167.
28. L. Li, Z. Hu, Y. Lu, C. Wang, Q. Zhang, S. Zhao, J. Peng, K. Zhang, S.-L. Chou and J. Chen, *Angew. Chem. Int. Ed.*, 2021, **60**, 13050–13056.
29. X. Wu, S. Qiu, Y. Liu, Y. Xu, Z. Jian, J. Yang, X. Ji and J. Liu, *Adv. Mater.*, 2022, **34**, 2106876.
30. B. Xiao, Z. Sun, H. Zhang, Y. Wu, J. Cui, J. Han, M. Li, H. Zheng, J. Chen, M. Cai, C. Ke, X. Wang, H. Liu, Z. Jiang, S. Zhang, D.-L. Peng, Z. Guo and Q. Zhang, *Energy Environ. Sci.*, 2023, **16**, 2153–2166.
31. B. Liu, Q. Zhang, U. Ali, Y. Li, Y. Hao, L. Zhang, Z. Su, L. Li and C. Wang, *Chem. Sci.*, 2022, **13**, 10846–10855.